NASA Contractor Report 4154

Distributed Feedback Lasers

I. Ladany, J. T. Andrews,
and G. A. Evans

CONTRACT NAS1-17351
JUNE 1988

NASA Contractor Report 4154

Distributed Feedback Lasers

I. Ladany, J. T. Andrews,
and G. A. Evans
David Sarnoff Research Center
Princeton, New Jersey

Prepared for
Langley Research Center
under Contract NAS1-17351

National Aeronautics
and Space Administration

**Scientific and Technical
Information Division**

1988

PREFACE

This Final Report covers work performed at the David Sarnoff Research Center from 19 June 1984 to 18 June 1986 under Control No. NAS1-17351 by the Optoelectronics Research Laboratory, B. Hershenov, Director. The Group Head was M. Ettenberg, the Project Scientist, Ivan Ladany, and the COTR was H. Hendricks, NASA Langley Research Center, Hampton, VA. Staff members and support personnel who contributed to this work in addition to the authors, and the areas of their contribution, are listed below.

N.W. Carlson	Spectroscopy
L.A. Carr	LPE and Photoluminescence
E. DePiano	Device processing
D.E. Devlin	SEM
D.B. Gilbert	Measurements
M.G. Harvey	Device processing
J.B. Kirk	Grating fabrication
E.R. Levin*	SEM
D.P. Marinelli	Diffusion
S.A. Siegel	High-frequency measurements
R.T. Smith*	X-ray diffraction
P.J. Zanzucchi*	IR absorption and reflection
D.T. Tarangioli	Device processing
M. Toda*	High-frequency mount design

* Member, Technical Staff

Table of Contents

List of Illustrations

List of Illustrations
(cont'd.)

List of Illustrations
(cont'd.)

List of Illustrations
(cont'd.)

List of Illustrations
(cont'd.)

List of Illustrations
(cont'd.)

SUMMARY

We have developed a ridge-waveguide distributed feedback laser in InGaAsP. These devices have demonstrated cw output powers over 7mW with threshold currents as low as 60 mA at 25°C. Measurements of the frequency response of these devices show a 3 dB bandwidth of about 2 GHz, which may be limited by the mount. The best devices have single-mode spectra over the entire temperature range tested with a side mode suppression of about 20 dB in both cw and pulsed modes. The design of this device, including detailed modeling of the ridge-guide structure, effective index calculations, and a discussion of the grating configuration are presented. Also, the fabrication of the devices is presented in some detail, especially the fabrication of and subsequent growth over the grating. In addition, we have designed and tested a high-frequency fiber-pigtailed package, which is a suitable prototype for a commercial package.

I. INTRODUCTION

Single-frequency diode lasers are highly desirable and even essential for a number of applications in fiber-optic communications. These include wavelength-division-multiplexing and high bit rate, long-haul communication systems. Single-frequency performance has been demonstrated with a number of conventional index-guided diode lasers; however, without some sort of frequency stabilization scheme, such operation is tenuous and mode hopping generally occurs. Under this program, the David Sarnoff Research Center has successfully developed a frequency-stabilized laser in InGaAsP operating in the 1.3- to 1.55-μm range.

The primary factors important in the design of this laser were low threshold current, high-speed modulation, and stability of the wavelength over as wide a range of operating conditions as possible. The two laser concepts that were considered were distributed feedback (DFB) lasers and distributed Bragg reflector (DBR) lasers. The DFB laser was chosen because, based on the literature, it appeared to have the lowest threshold current. This was presumably due to the coupling losses to the grating in the DBR configuration. A ridge-waveguide structure was chosen because of its excellent high-speed characteristics, the ease of incorporating a grating, and the fact that it could be grown by both liquid phase and vapor phase epitaxy.

The ridge-guide DFB lasers we have fabricated have obtained single-mode cw output powers over 7 mW with threshold currents as low as 60 mA at 25°C. The best devices have single-mode spectra over the entire temperature range tested with a side mode suppression of 20 dB in both cw and pulsed operation. Measurements of the frequency response of these devices show a 3 dB bandwidth of about 2 GHz, which may be limited by the mount.

This report describes in detail both the device design and fabrication as well as the device results. For the design, we have used our extensive modeling capabilities to refine the ridge-guide geometry and also to calculate the effective index in the laser, which is required for determining the best grating period. The fabrication of the grating is discussed in some detail, especially with regards to obtaining the optimum grating shape and depth by chemical etching. In addition, the problems associated with regrowth over the grating is discussed and our solutions described. There is also a section in this report that describes studies done

on using Cd diffusion as an alternative to Zn, which is used extensively in InP devices, but which causes a number of problems. In the section on device results, we present power curves, spectra, field patterns and high-frequency bandwidth measurements. In this section, we also describe the variety of spectra we have observed during this program and we discuss some of the mechanisms responsible for obtaining single-frequency operation from a DFB laser. Finally, the last section of this report presents a high-frequency, fiber-pigtailed laser package, which was designed and demonstrated under this program.

II. PRINCIPLES OF DFB LASERS

Because of the broad gain bandwidth of diode lasers, it is necessary to incorporate a frequency selective element in the cavity in order to obtain single wavelength operation under a wide range of operating conditions. The method of choice is to use a Bragg reflecting grating, which reflects only in a relatively narrow wavelength band, as the feedback element. The two configurations in which a Bragg reflector is typically used are the distributed Bragg reflector (DBR) laser, in which the grating is external to the gain region, and the distributed feedback (DFB) laser, in which the grating is formed in the gain region. Although single-line emission has been achieved with both DBR and DFB lasers, it was decided to concentrate on the DFB structure, mainly because it seemed to yield the best performance on the basis of published information.

The basic idea of the distributed feedback (DFB) laser is illustrated in Fig. 1, which shows the usual Fabry-Perot type of feedback (reflection at the cleaved laser ends) and grating feedback (the return of radiation by scattering from the grating protrusions). This back-scattering process is distributed along the cavity (which explains the origin of the name). The relationship between the grating period P and the wavelength at which the light is reflected by the grating is given by the expression

$$P = m\lambda_0/(2\, n_{eff}), \tag{1}$$

where n_{eff} is the effective index of the waveguide, λ_0 is the vacuum wavelength, and m is an integer denoting the order of the grating.

Most DFB lasers use a second-order grating as a compromise between effectiveness (i.e., optimizing feedback) and ease of fabrication, but it is also possible to make a first-order grating, especially at the longer wavelengths. In general, because of the losses due to radiation normal to the waveguide plane that occurs with a second-order grating, a laser with a first-order grating is expected to have a lower threshold gain and thus a lower threshold current. The fact that the second-order grating allows an emission at right angles to the grating plane was originally thought to be an undesirable loss mechanism. The loss, however, is not significant, as evidenced by the low threshold currents observed with some second-order grating devices. Furthermore, the loss is thought to be a powerful

mechanism for mode selection [17]. All work done in this program was based on second-order gratings.

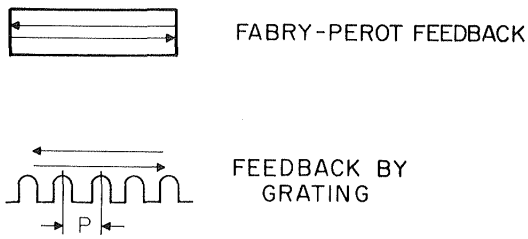

Figure 1. A comparison between Fabry-Perot feedback and grating feedback.

The operation of DFB lasers is generally understood through the wavelength selection process described by Kogelnik and Shank [10]. While it might be reasonable to expect the grating to select a single wavelength and thus provide single longitudinal-mode lasers, the situation is actually somewhat more complex.

As shown in Fig. 2, several modes (lines) having different threshold gains are allowed. Of these, the closest two, centered symmetrically about the Bragg frequency, have the lowest threshold gain and are expected to be the ones excited. The modes of the DFB laser occur at those combinations of wavelength and gain where the transmission through the laser structure diverges. These wavelengths correspond to minima in the reflectivity of the Bragg grating incorporated in the laser. The positions of the minima depend on the strength and length of the grating. This is analogous to a Fabry-Perot laser, in which case the modes occur at the minima in reflectivity of the Fabry-Perot structure viewed as an optical waveguide element.

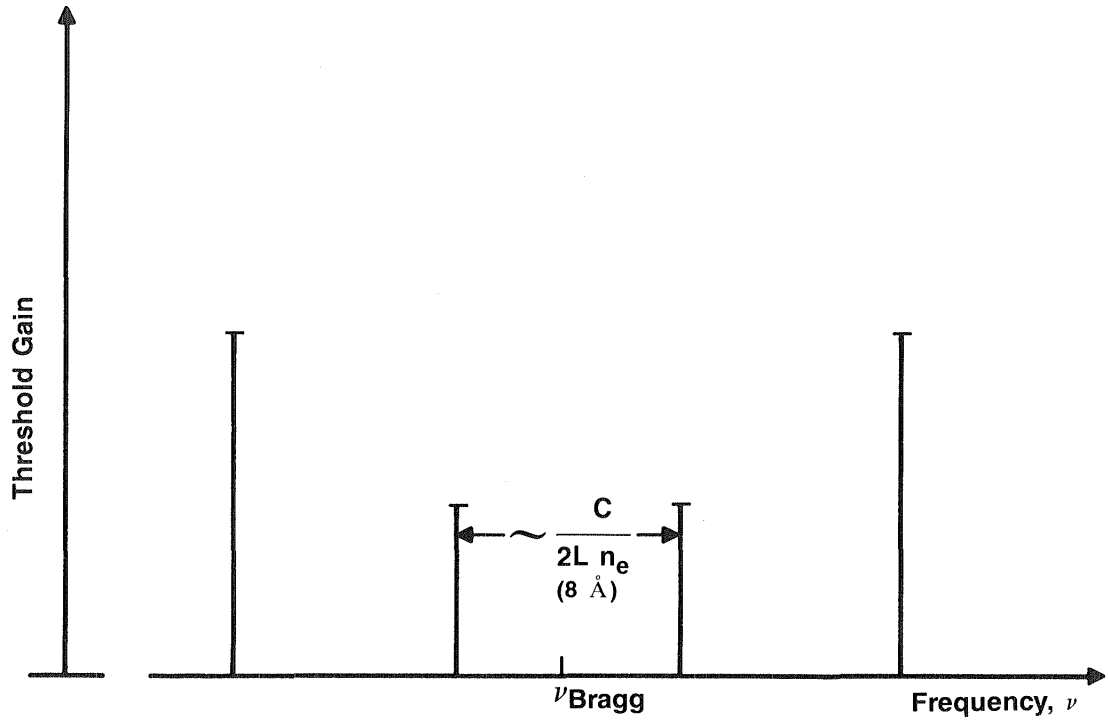

Figure 2. Allowed modes of a DFB laser.

In practice, one often observes the appearance of two lines, in agreement with this model, and the problem becomes one of understanding how to excite only one line. It turns out that a certain percentage of lasers are true single-line emitters, achieving this state either because of radiation loss or some break in the grating periodicity. This could be caused by reflections off the facets or by non-uniformities in the growth layers across the device length. The mode selection process is discussed more extensively in the section describing our device results.

III. CHOICE OF LASER STRUCTURE

Given the use of a DFB-type cavity to obtain wavelength-stabilized operation, there remains the question of the geometry to be used for the device. Gain-guided lasers are not well suited for DFB action, because the guiding effect and, thus, the effective index depend on the bias current. In index-guided lasers, although the injected current also affects the index, the guiding is largely independent of current, so that the effective index is more nearly constant. Another unwanted effect of gain-guided lasers is that they generally have higher threshold currents.

There are many index-guided structures that consist of an active layer completely surrounded by lower-index material, which belong to the general class of buried heterostructures (BH). The lowest threshold DFB lasers reported were obtained by use of a dual-channel planar buried-heterostructure (DCPBH) geometry.

However, this structure suffers from a modest frequency response, caused by the capacitance associated with the blocking layers needed to restrict the current flow to the active region. It thus appeared that the ridge-guide, even though it has a somewhat higher threshold current than the DCPBH, would offer the best combination of threshold and frequency response. Another reason for favoring this structure was that even though all this work was carried out with liquid-phase epitaxial growth (LPE), it was expected that eventually a vapor-phase system would be used, and a geometry that could also be fabricated by vapor-phase epitaxy (VPE), such as the ridge-guide, was preferred.

It should be added that since the work under this contract was completed, there have been several reports of DCPBH lasers incorporating semi-insulating, Fe-doped, InP blocking layers in place of the reverse junction layers. Because of the very low capacitance associated with the semi-insulating material, these lasers have exhibited outstanding high-frequency performance (several GHz). As a result, it might be worthwhile to reconsider the use of the DCPBH structure for any future work.

IV. BASIC PRINCIPLES OF RIDGE-GUIDE LASERS

The ridge-guide (RG) laser (Fig. 3) obtains its index guiding in a way fundamentally different from that occurring in BH lasers. It belongs to the class of strip-loaded film guides and functions because a waveguide containing a ridge of material will develop a higher effective index under the ridge than in those portions of the waveguide not covered by the ridge.

The details of the fabrication of the ridge-guide laser are given later in this report. Briefly, the ridge-guide structure consists of an InGaAsP active, a InP spacer and an InGaAsP waveguide layer grown on an n-type InP buffer and substrate. After forming the grating on the waveguide layer, an InP p-cladding layer and a heavily doped p-InGaAsP contact layer are grown. For lasers emitting at 1.3 μm, the composition of the active and waveguide layers correspond to bandgaps of 1.3 and 1.1 μm; for the 1.55-μm lasers, they are 1.55 and 1.3 μm, respectively. Finally, the ridge is formed by photolithography and subsequent wet etching of the of the contact and p-cladding layer. The net effect is a strip-loaded waveguide that consists of the active, spacer and waveguide layers as the guiding layers, the InP substrate, and a ridge of InP. As we will see below, the effective index of this guide under the ridge is larger than the effective index outside of the ridge, leading to positive index guiding in the lateral direction (parallel to the layer interfaces).

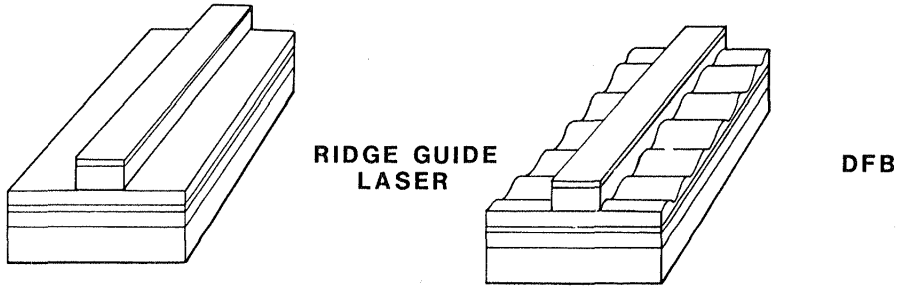

Figure 3. Ridge-guide laser geometry and its DFB version.

The purpose of the InP spacer layer is two-fold. First, in the 1.55-μm lasers, it is required to prevent the meltback of the active layer during the growth of the waveguide layer. Also, in lasers of both wavelengths, it may improve the confinement of carriers in the active layer. This is because the barrier height between the active and waveguide layers may not be sufficient to prevent electrons from leaking over the barrier. However, since the spacer layer may also hinder the optical coupling to the grating, it was not used on all 1.3-μm lasers.

In this section we describe our modeling of the ridge-guide structure. The basic parameters that are calculated are the waveguide effective index in the laser and the field profile. From this we obtain a number of important quantities, such as the degree of lateral index guiding, the optical confinement factor, both in the active layer and under the ridge, and the near- and far-field intensity patterns. The degree of lateral optical confinement is a crucial parameter in the ridge-guide laser because it determines both the threshold and the mode behavior. The field-intensity patterns are important not only as a property to optimize to obtain the desired beam shape, but also as a means to compare the model to the actual device results. By varying the layer thicknesses and composition, one can optimize the laser structure based on this model. In addition, the effective index obtained in the calculations is needed to determine the proper grating period.

The effective index is defined by the equation

$$n_{eff} = \frac{\beta}{k_0} \tag{2}$$

which is the ratio of the guide wave number (β) to the free space wave number (k_0). This ratio is determined by solving the wave equation, with appropriate boundary conditions, for the region of interest. In the case shown in Fig. 4, the boundary conditions involve multiple layers including the active region, a spacer layer, the waveguide region, and the InP regions. Such solutions are not difficult, but can get cumbersome for multiple layers. A computer model, which was partly developed at the David Sarnoff Research Center, is used for the calculations.

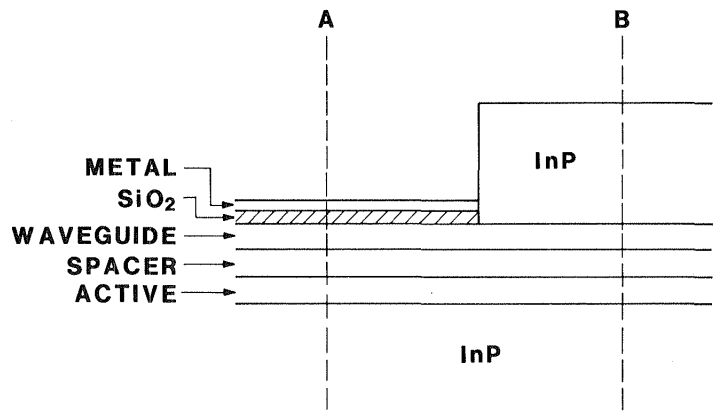

Figure 4. Generalized structure of the ridge-guide DFB laser.

Generally, the effective index calculation is made for expected or measured ranges of active-layer thicknesses, epilayer refractive indices, and lasing wavelengths. The electric field distribution perpendicular to the p-n junction $E_y(x)$ in the ridge region and outside the ridge region is calculated separately, assuming each region is infinitely wide. The electric field distribution perpendicular to the p-n junction $E_y(x)$ is obtained by solving the one-dimensional wave equation:

$$\partial^2 E_y/\partial x^2 + (\varepsilon_r k_o^2 - \beta^2)E_y = 0 \tag{3}$$

with the usual boundary conditions on E and H at the epilayer interfaces, using an algorithm for calculating complex modes in plane-layered, complex dielectric structures [16]. Here, $\varepsilon_r(x)$ is the complex relative-electric permittivity in either the ridge region or outside the ridge region, $k_o = 2\pi/\lambda_o$, and λ_o is the free-space wavelength. An $\exp[i(\beta z - \omega t)]$ longitudinal and time variation of the electric field is assumed. The real part of the complex index of refraction, $n^*(x)$, is the real part of the square root of the complex relative electric permittivity. The effective index n_{eff} of region A (inside the ridge region) and B (outside the ridge region) in Fig. 5 is

$$n^i_{eff} = Re(\beta^i/k_0) \qquad i = A,B \tag{4}$$

and the mode loss of region A and B in Fig. 1 is:

$$\alpha^i = 2\, k_0\, Im(\beta^i/k_0) \quad i = A,B \tag{5}$$

The theoretical calculations of the electric field and near-field intensity distributions are both normalized according to

$$1 = \int_{-\infty}^{\infty} E_y(x)\, E^*_y(x)\, dx \tag{6}$$

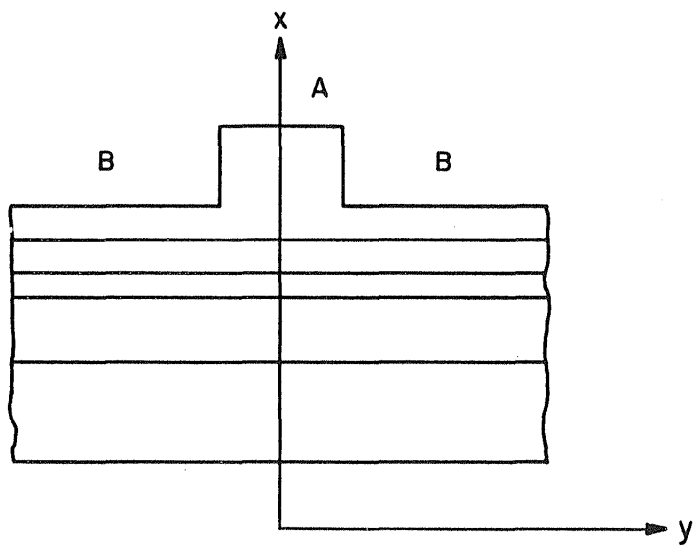

Figure 5. Geometry used in the analysis of ridge waveguide.

The far-field intensity distribution $I(\theta)$ is calculated from the complex electric field distribution according to

$$I(\theta) = \left| g(\theta) \int_{-\infty}^{\infty} E_y(x) \exp(i \sin\theta k_0 x) dx \right|^2 \Bigg/ \left| g(0) \int_{-\infty}^{\infty} E_y(x)\, dx \right|^2 \tag{7}$$

where $g(\theta)$ is the obliquity factor [13].

The confinement factor Γ is defined for any layer as

$$\Gamma_{\text{layer}} = \left| \int_{\text{layer}} E_y(x) E^*_y(x)\, dx \right| = \int_{-\infty}^{\infty} E_y(x) E^*_y(x)\, dx \tag{8}$$

As an example, Fig. 6 gives the effective index under the ridge for the fundamental mode in the perpendicular direction for active-layer thicknesses of 0.1, 0.15, 0.2, 0.25, and 0.3 μm as a function of waveguide thickness, for an emission wavelength of 1.55 μm. Fig. 7 is a plot of the active-layer confinement factor for the same parameters as Fig. 6.

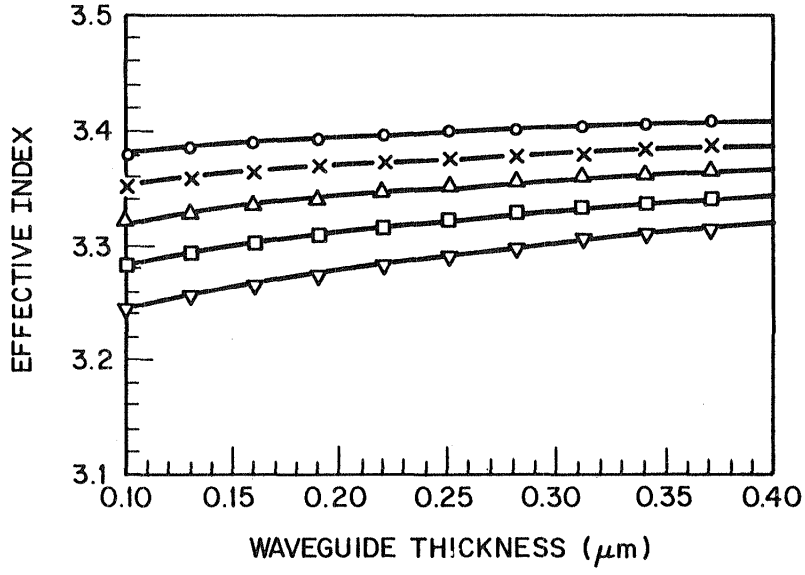

Figure 6. Effective index perpendicular to the junction inside the ridge region as a function of waveguide thickness. The parameter is the active-layer thickness: 0.3 μm (o), 0.25 μm (x), 0.2 μm (Δ), 0.15 μm (£), and 0.1 μm (∇). Active-layer composition 1.55 μm, waveguide layer composition 1.3 μm.

To calculate the two-dimensional mode, we apply the effective index approximation. In this method, we assume that the guiding in the lateral direction can be described by the solutions to a three-layer planar guide with a film index equal to the effective index of the transverse mode under the ridge. Similarly, the substrate and cover indices are taken equal to the lower effective index of the transverse mode outside the channel.

Fig. 8 is a plot of the effective index of the two-dimensional mode as a function of ridge width for the geometry shown in Fig. 9, which has an active layer of 0.15 μm and a waveguide thickness of 0.2 μm. For ridge widths greater than 3 μm, the decrease in the normalized, two-dimensional longitudinal wave vector (effective index) from that of the one-dimensional case (Fig. 6) is less than 0.005. This minor change in effective index between the one-and two-dimensional cases corresponds to only a 7-Å increase in the second-order Bragg grating period (or 3.5 Å for a first-order Bragg grating). Therefore, for ridge widths of 3 μm or greater, the effective index curves of Fig. 5 provide effective index values of sufficient accuracy for calculating grating periods.

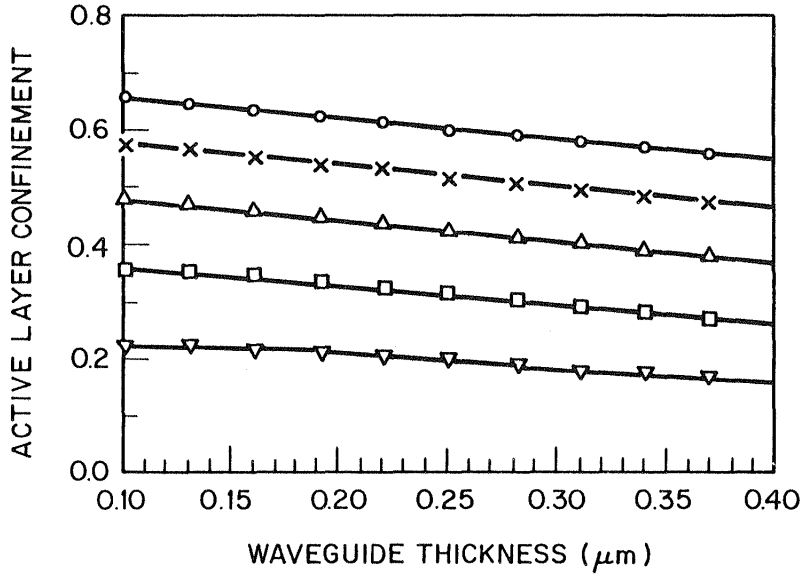

Figure 7. Active-layer confinement inside the ridge region as a function of waveguide thickness. Other parameters as in Fig. 6.

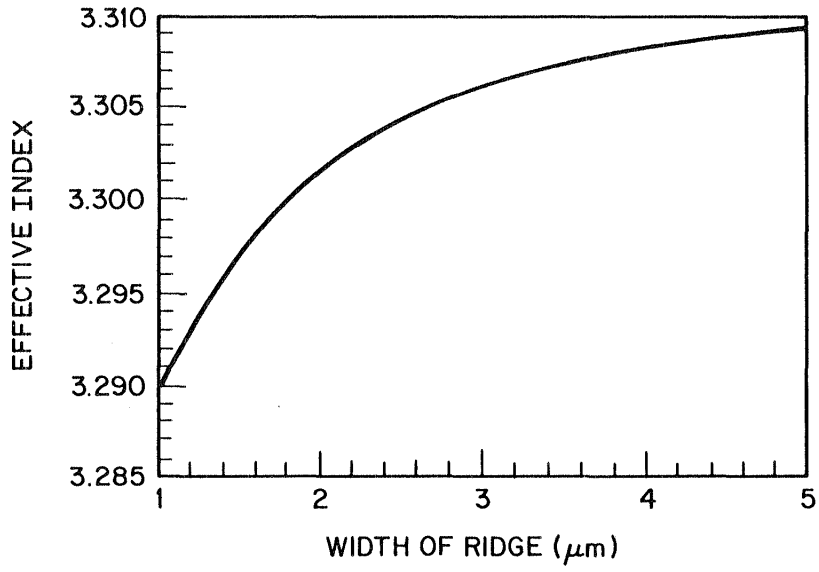

Figure 8. Effective index for the fundamental mode of the two-dimensional structure shown in Fig. 9, as a function of ridge width.

The effective index curve in Fig. 8 is that of the "cold cavity." The effect of gain-induced index depression has not been included. In AlGaAs devices, the effect of gain-induced index depression typically reduces the two-dimensional longitudinal propagation constant (effective index) by 0.001. The same change in 1.3- or 1.55-μm devices would only increase the second-order grating period by 1 Å (0.5 Å for a first-order grating). The error introduced in the grating period by this effect is much smaller than the uncertainties in the calculated period resulting from experimental uncertainties. Thus, it is not a significant effect. There are some data in the literature [14] on the index depression for 1.3- and 1.55-μm devices, and we will include this effect in future calculations. Based on these calculated effective indices, a typical grating period for 1.55-μm devices is 4687 Å (second-order) and 2349 Å (first-order). Either of these can easily be accomplished by the grating fabrication facility at the David Sarnoff Research Center.

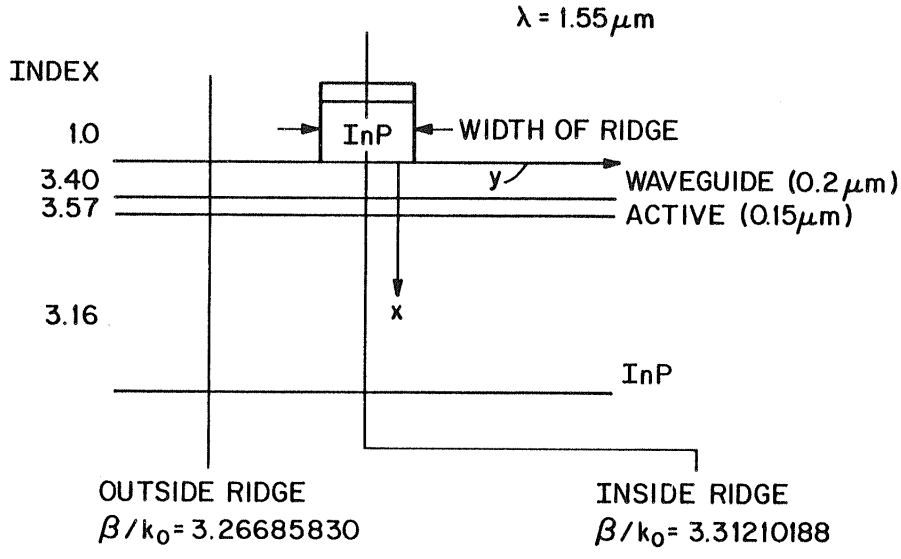

Figure 9. Geometry of the ridge structure used in the analysis. Refractive indices and effective indices inside and outside ridge are also shown.

Figure 9 also shows the calculated effective index inside and outside the ridge structure. The lateral index step is 4.52×10^{-2}, which agrees with previously published "good" design values [1]. The point here is that the lateral index step should be large enough so that any gain-induced index depression under the ridge will not significantly affect the degree of lateral guiding, as this would cause the field to change as the current to the laser were changed. Also, the step should not be so large that more than one mode will have significant gain for a ridge width that can be easily fabricated.

Figure 10 is a plot of the ratio of the lateral mode energy that is confined within the boundaries of the ridge to the total mode energy, for the geometry in Fig. 9. For narrow ridge widths, this curve suggests the possibility of fabricating the grating after all the layers are grown in a single growth and the ridge is defined. In this case, the grating would appear only in the regions outside the ridge. The interaction of the grating would then be with the lateral mode energy outside the ridge which may be sufficient for DFB action. Another way of looking at this is that since some of the mode energy is outside the ridge, a grating in this

region would cause a periodic disturbance in the effective index of the mode. Since the ridge confinement decreases with decreasing ridge width, a narrower ridge would effect a larger coupling to a grating present only outside the ridge.

Figure 11 is the near-field intensity perpendicular to the junction inside the ridge region. The InP/waveguide layer interface is located at x = 0.

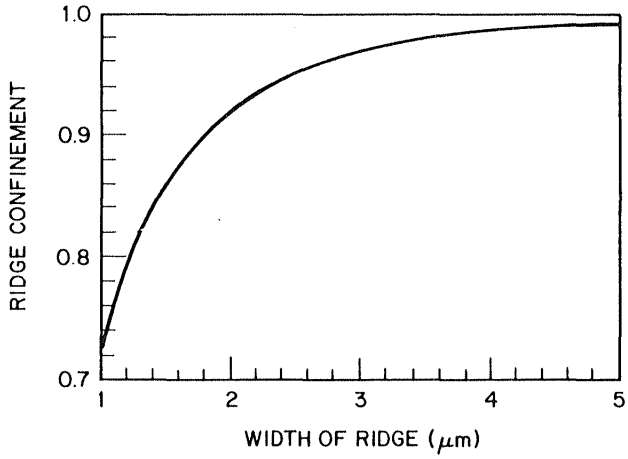

Figure 10. Confinement factor, or ratio of mode intensity within the ridge boundaries to the total mode intensity, as a function of the ridge width. Active-layer thickness is 0.15 μm and the waveguide thickness is 0.2 μm.

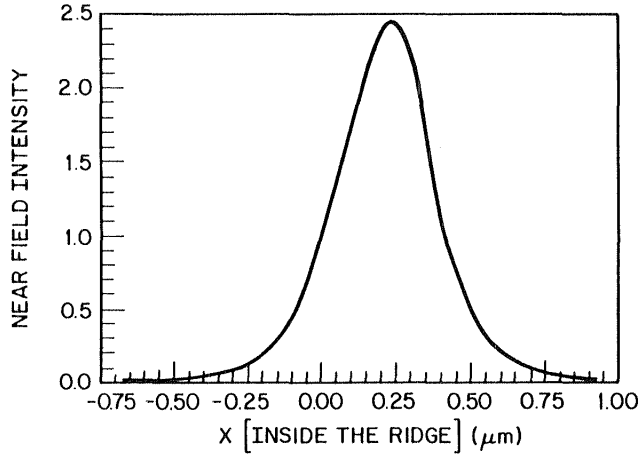

Figure 11. Near-field intensity perpendicular to the junction inside the ridge region. x = 0 is the location of the top of the waveguide in Fig. 9.

Figure 12 is the corresponding near-field phase that is extremely flat (the vertical axis is multiplied by 10^{-10}). In this ridge structure, all phase fronts (perpendicular to the junction inside and outside the ridge, and parallel to the

junction) are extremely flat. Figure 13 is the perpendicular far field corresponding to the structure shown in Fig. 9, which has a FWHM beam divergence of 65°.

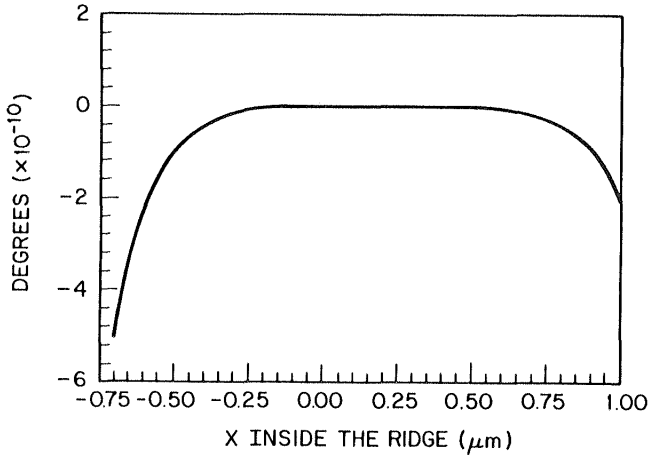

Figure 12. Phase of the near-field intensity shown in Fig. 11.

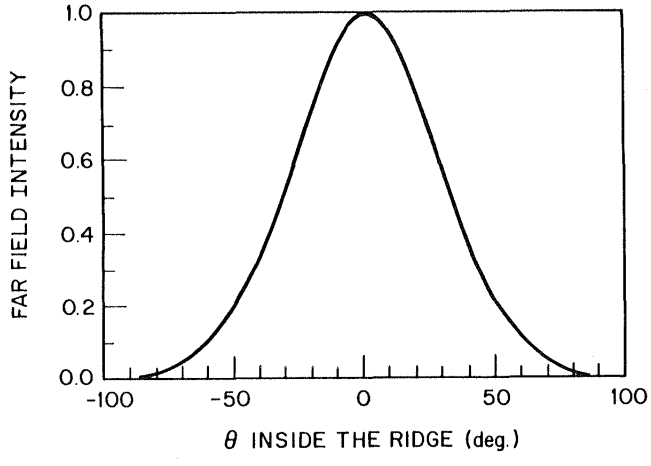

Figure 13. Perpendicular far-field pattern for the structure shown in Fig. 9 and whose near-field pattern is shown in Fig. 11.

The perpendicular near-field intensity outside the ridge is shown in Fig. 14. Again, the InP/waveguide interface is at x = 0. The field intensity at the top of the waveguide in the region outside the ridge is reduced only to about 30% of that inside the ridge (Fig. 11). The corresponding far-field pattern for the near-field intensity shown in Fig. 14 is given in Fig. 15. The FWHM beam divergence of 71° outside the ridge region is greater than that inside the ridge region because the near-field spot size is smaller outside than inside the ridge. However, because the

lasing spot is primarily confined to the ridge region, the experimentally measured far-field will nearly correspond to that inside the ridge region.

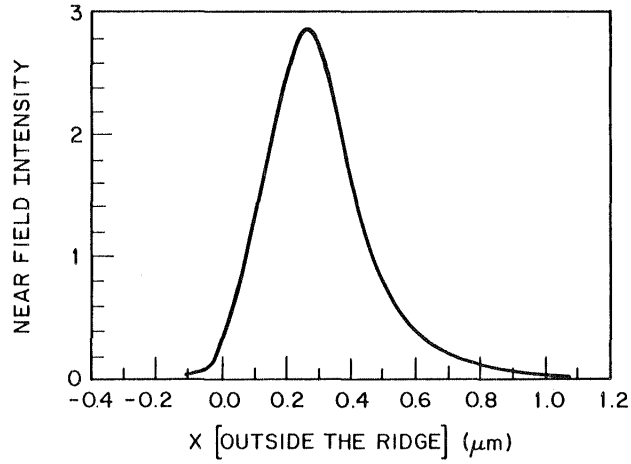

Figure 14. Near-field intensity perpendicular to the junction outside the ridge region. As before, x = 0 is the location of the top side of the waveguide in Fig. 9.

Figure 16 is the near-field pattern parallel to the junction for the geometry shown in Fig. 9 with a ridge width of 3 μm. The left-hand edge of the ridge is at x = 0. Figure 17 is the far-field intensity pattern corresponding to the near-field intensity distribution of Fig. 16, for which a 23° FWHM beam divergence in the parallel direction is calculated.

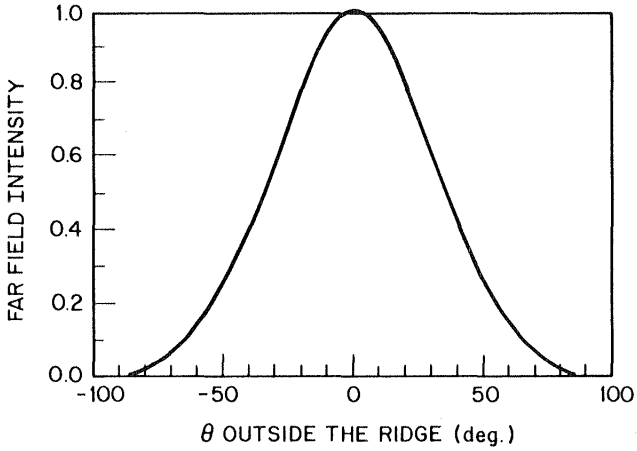

Figure 15. Far-field pattern perpendicular to the junction corresponding to the near-field pattern in Fig. 14.

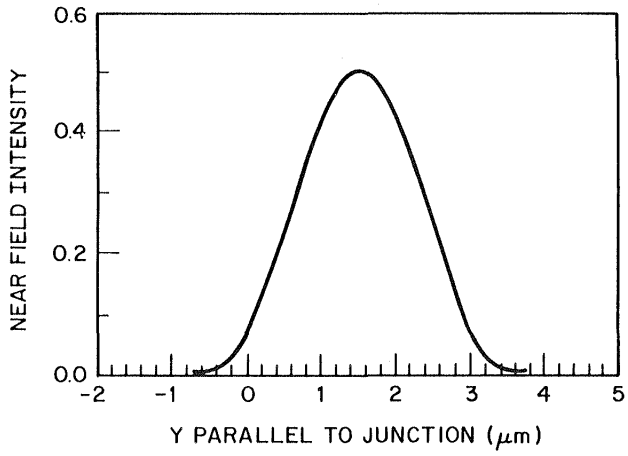

Figure 16. Near-field intensity pattern parallel to the junction for the geometry in Fig. 9, with a ridge width of 3 μm.

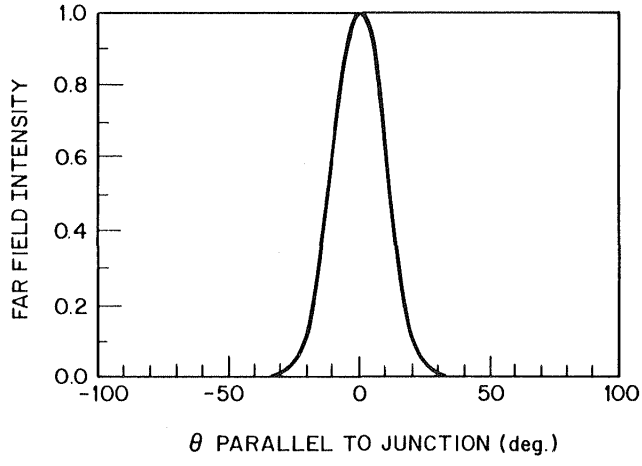

Figure 17. Far-field intensity pattern parallel to the junction for the geometry in Fig. 9, for ridge width of 3 μm.

Several calculations of the lateral index step in a 1.3-μm ridge-guide laser are given in Fig. 18. These are obtained by subtracting n_{eff} in region A from n_e in region B, and show how the lateral index step depends on the thickness of the various layers involved. Included in the figures are calculations for the case of an InP spacer layer between the active and the waveguide layers. This spacer improves the transverse carrier confinement but may affect the lateral index step or the mode-to-grating coupling coefficient. Lateral confinement also includes carrier and current confinements, and it must be accepted that these are somewhat smaller than in, say, the buried-crescent (BC) form of BH lasers.

While current confinement is weaker in the ridge guide because there are no blocking layers that channel the current to the active region, the absence of these blocking layers was one of the reasons for the choice of this geometry. Thus, a slightly reduced current confinement is acceptable as part of the tradeoff to achieve a higher frequency response. The carrier confinement suffers because of the absence of a lateral heterojunction boundary. A perspective on the computed values of the lateral index step can be obtained by noting that the lowest threshold lasers of the BH-type have a lateral index step (equal to the transverse index step) of 0.3. Thus the present value, which is less than 0.05, seems very low. Nevertheless, as discussed earlier, it is adequate for index-guided lasers, and it has the advantage of allowing a wider ridge before the onset of higher-order modes.

The weakest point of this structure is the loss of carriers in the lateral direction. The best approach for dealing with this loss is to make the active layer as thin as possible, on the order of 0.1 μm.

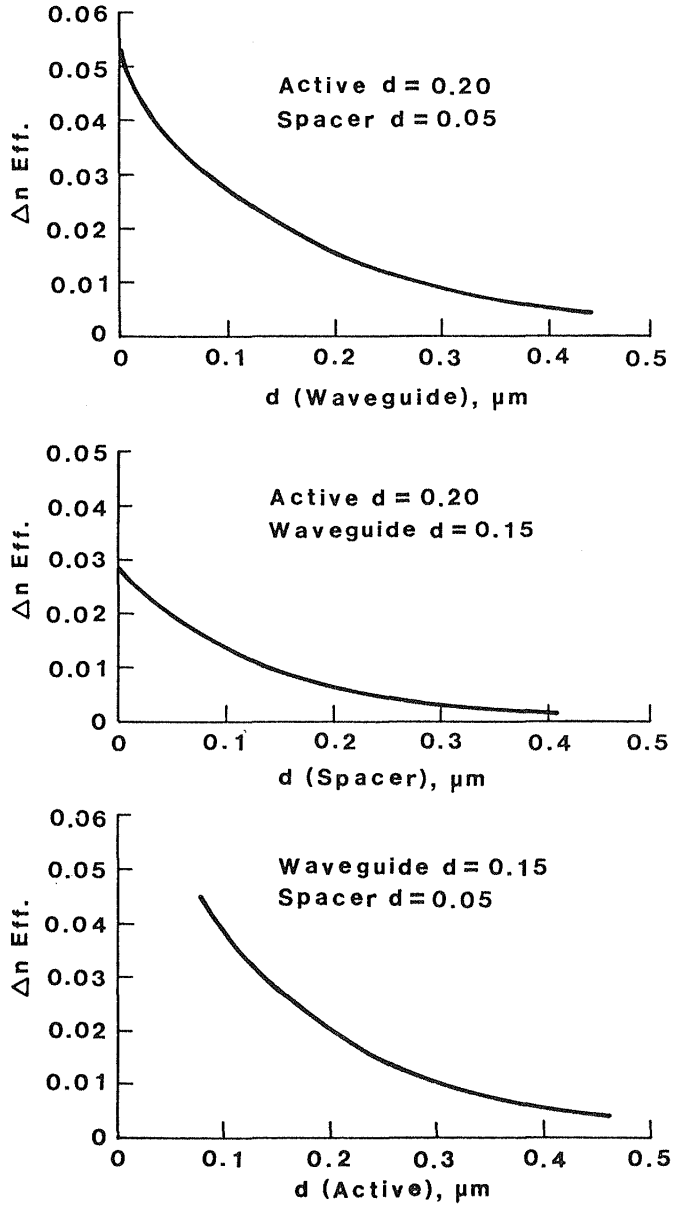

Figure 18. Lateral index step in multilayered ridge-guide laser. The thickness of various layers is the variable; the other layers are held constant at the indicated thickness.

Figures 19 through 21 present the results of effective-index calculations for a four-layer waveguide, in which the outer layers are InP and the active- and waveguide-layer thicknesses are as indicated in the figures. These plots are

made for an active-layer bandgap wavelength of 1.3 μm and a waveguide-layer bandgap wavelength of 1.1 μm.

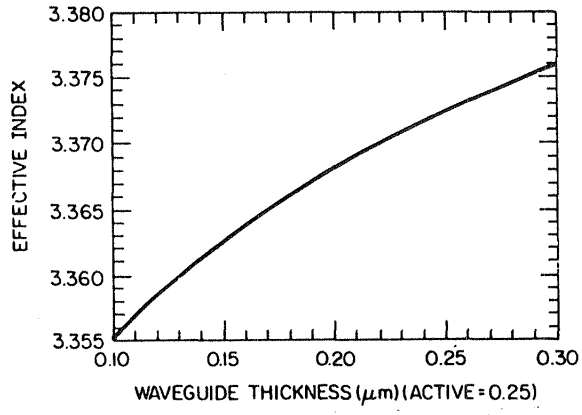

Figure 19. Effective indices calculated for a four-layer waveguide at 1.3 μm, the two outermost layers being infinitely thick InP; the active-layer thickness is 0.25 μm.

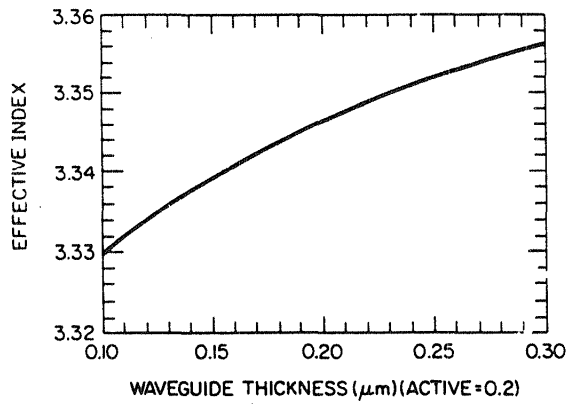

Figure 20. Same as Fig. 19, but with an active-layer thickness of 0.20 μm.

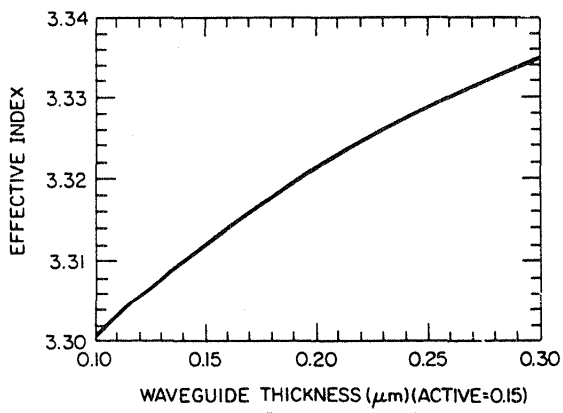

Figure 21. Same as Fig. 19, but with an active-layer thickness of 0.15 μm.

V. EFFECTIVE INDEX AND THE GRATING PERIOD

The second-order grating period P for DFB is calculated from

$$P = m\lambda_o/(2\ n_{eff}) \tag{9}$$

where λ_o is the free-space wavelength, m is the grating order (and is equal to 2 for second-order), and n_{eff} is the real part of the complex effective index of the laser mode. The complex effective index of the laser mode is calculated numerically, as discussed above, based on an algorithm [16] for calculating dielectric structures. The inputs to the numerical algorithm are the thicknesses of all the epilayers both inside and outside the ridge region, the index of refraction and loss of each epilayer and the substrate, the width and shape of the ridge, and the lasing wavelength of the device.

The epilayer thicknesses and ridge geometry are obtained from measuring layer thicknesses from micrographs of both cleaved cross sections and one-degree, angle-lapped cross-sections. The photoluminescence data for each epilayer is converted to the lasing wavelength that is used to determine refractive index values.

The grating period must be ascertained from the grating equation [Eq. 9], which requires knowledge of the emitted wavelength and the effective index. The effective index thus plays an even more important role than in the lateral index step discussed previously. The effective index can be computed from a knowledge of the structure and the refractive indices of the layers.

The major uncertainty in the effective index calculation is determining the refractive index of the layers. Interpolation procedures for calculating the index have been criticized by some writers, and methods based on the Kramers-Kronig relations have been criticized by others. Since the index depends on the change in absorption throughout a wide spectral region, only experimentally measured index values can be trusted, and these only for the material on which they were measured. We have made a survey of published indices and have compiled a set of curves (Fig. 22) of the index we use in our calculations.

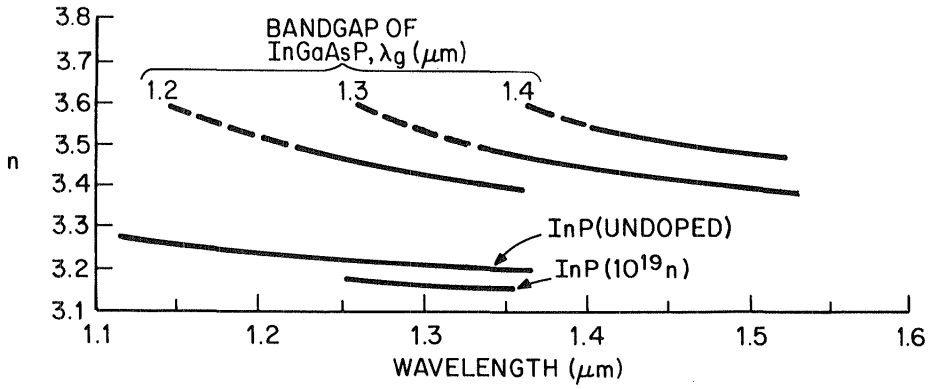

Figure 22. Refractive index of InP and of various compositions of InGaAsP. The compositions are defined by the bandgap expressed in terms of wavelengths.

Another method we have used to determine the refractive index of the materials discussed in this section is a model of Henry et al. [9], which was developed to fit their measurements. This is a mathematical model using a two-oscillator dispersion function. The index is given by

$$n^2 = 1 + \left\{ \frac{A_1}{1 - \left(\frac{E}{E_p + E_1}\right)^2} + \frac{A_2}{1 - \left(\frac{E}{E_p + E_2}\right)^2} \right\} \tag{10}$$

where E_p is the photoluminescence peak energy, E is the energy corresponding to the wavelength of interest, A_1, A_2, E_1, and E_2 are fitting parameters. We have used values of these parameters obtained by Henry et al. [9] from fitting their data. The values they obtain are

$$\begin{aligned} A_1 &= 13.3510 - 5.4554\,E_p + 1.2332\,E_p^2 \\ A_2 &= 0.7140 - 0.3606\,E_p \\ E_1 &= 2.5048 \text{ eV} \\ E_2 &= 0.1638 \text{ eV} \end{aligned}$$

A plot of refractive indices based on this equation and parameters is given in Fig. 23. No significant differences arise from the use of these index values instead of the ones shown in Fig. 22. This formulation has the great advantage of being available in a closed form that can be written into a computer program, and is thus available in the course of computations.

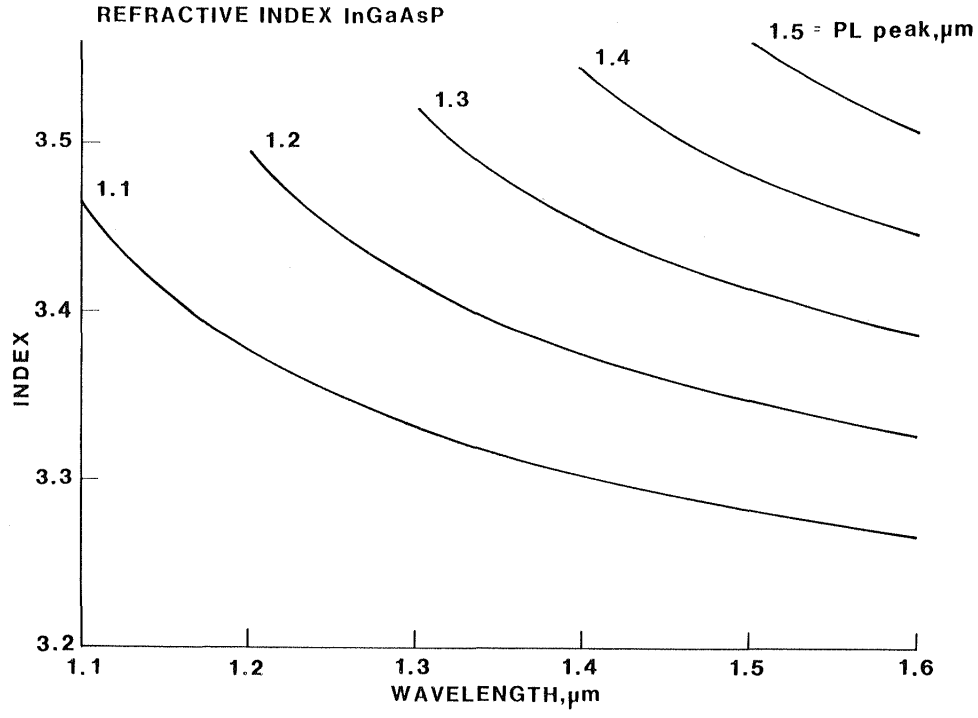

Figure 23. Refractive index of InGaAsP as a function of photon wavelength and material bandgap wavelength (taken to be the wavelength of the photoluminescence peak). After Henry et al.

The procedure used to calculate the grating period in this program was to measure the layer bandgaps (by photoluminescence) and the thicknesses on each wafer and then carry out the effective-index calculation for the exact case under consideration. The end result of these calculations, the effective index for a particular wafer is then used together with the expected lasing wavelength to determine the grating period.

VI. PHOTOLUMINESCENCE MEASUREMENTS

As discussed above, an estimate of the layer compositions and the completed device's expected emission wavelength is necessary to calculate the grating period. This is available from the knowledge of the melts used to grow the active layers, but such estimates tend to be very uncertain. An improved estimate can be obtained by assessing the grown wafers by photoluminescence (PL), after the first growth series is completed. At this stage, the wafers usually have an overgrowth of an active layer at 1.3 μm followed by the waveguide layer at 1.1-μm bandgap wavelength (or an active layer at 1.55 μm followed by a waveguide layer at 1.3 μm). Sometimes, these are inverted, and sometimes there is an InP layer sandwiched between these two layers. The important layer to examine is the active layer, but it is also useful to determine the bandgap of the waveguide layer. Typical PL spectra are shown in Figs 24, 25, and 26. Table I presents the peak position obtained from them.

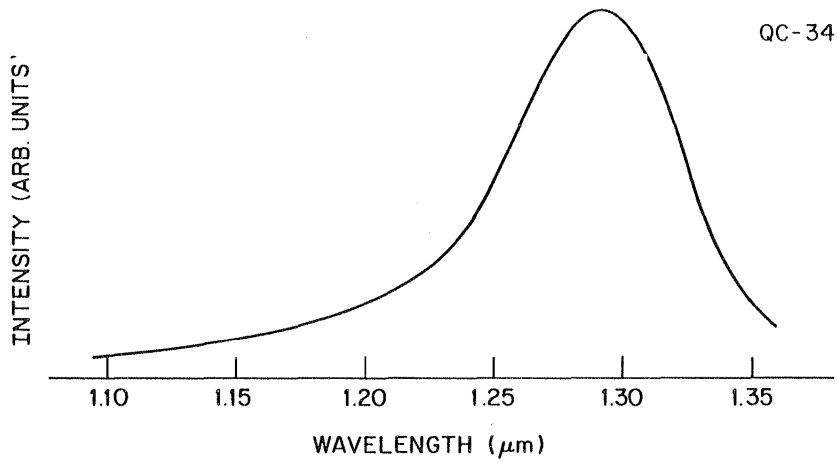

Figure 24. Photoluminescence of the 1.1-μm layer grown on top of 1.3-μm layer, grown on InP. There is no measureable contribution at 1.1 μm.

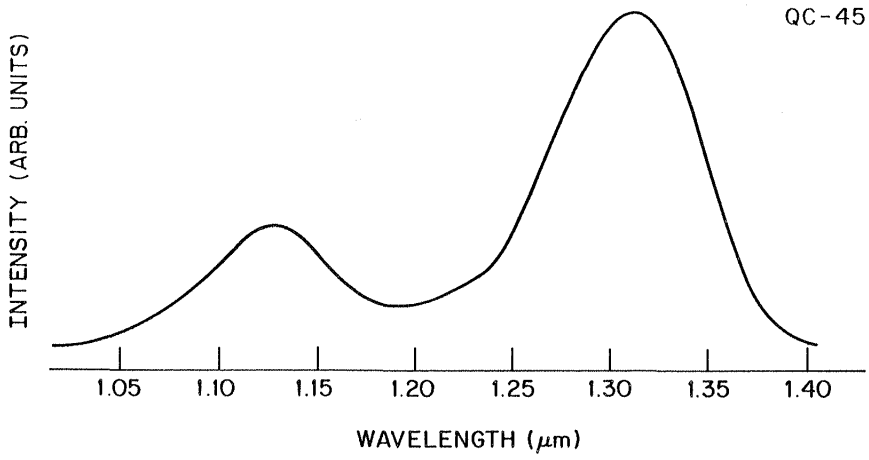

Figure 25. Photoluminescence of the Fig. 24 structure, except that the two layers are separated by a layer of InP.

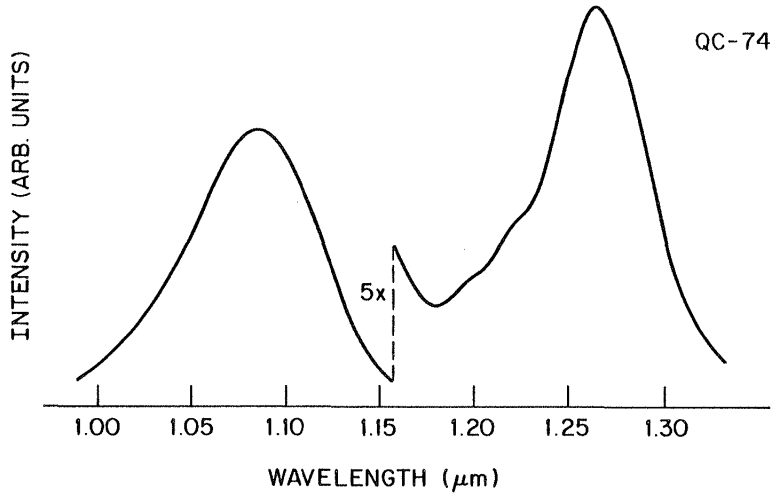

Figure 26. Photoluminescence of Fig. 25 structure, except that the order of the two quaternary layers is inverted.

These results show that no contribution is obtained from the surface 1.1 μm layer for sample QC-34, but this layer does contribute to the measured signal if the two layers are separated by a layer of InP as in QC-45. This is due to the complete trapping of the generated 1.1-μm radiation in the 1.3-μm layer, where it is converted into 1.3-μm radiation. The reappearance of the 1.1-μm radiation in sample QC-45 is explained by the partial reflection of the 1.1-μm radiation at the 1.1-to-InP boundary, thus increasing the amount of 1.1-μm radiation available for measurement.

Table I. Photoluminescence of Typical LPE Layers

Wafer Number	Structure (Starting at Surface)	Peak Wavelength (μm)	Intensity Ratio ($\lambda = 1.1/\lambda = 1.3$)
QC-34	1.1/1.3	1.297	--
QC-45	1.1/InP/1.3	1.135 & 1.314	30/74
QC-74	1.3/InP/1.1	1.267 & 1.088	63/18

For similar reasons, both peaks are observed in sample QC-74. However, the intensity ratio for sample QC-74 favors the 1.1-μm output, contrary to expectations; the system behaves as if the deeper lying material is favored. The most likely explanation for this is nonradiative recombination of carriers at the wafer surface, which would reduce the PL contribution of surface layers. The trapping (or photon pumping) together with nonradiative recombination at the free surface explain the observed spectra qualitatively. It appears that the surface layer, if it is higher in bandgap, cannot be easily measured by photoluminescence.

To determine the accuracy of the grating calculations, we have compared the calculated effective index to experiment. With DFB lasers, the actual effective index can be obtained by dividing the emitted wavelength by the grating period (for a second-order grating). Table II compares the calculated (or estimated) effective index to the measured effective index for several DFB laser wafers grown under this program. At present, these calculations are not very accurate. Also shown are threshold currents for lasers made from these wafers. Agreement between the two effective-index values correlates with threshold current, presumably because, if the effective index is far enough away, the laser will be forced to oscillate somewhere down the gain curve away from the peak value.

There are several reasons why it is not always easy to obtain the correct effective index. Foremost is the difficulty of measuring the layer thickness, especially since this thickness varies in both a systematic and a random fashion across the wafer. This is the main reason that VPE growth is preferred for the fabrication of DFB structures. Another problem arises in estimating the grating amplitude, and this must be considered in determining the thickness to be used in calculating the effective index. Finally, the bandgap as measured by photolumi-

nescence is not always a reliable indicator of the peak of the gain curve or the unforced laser emission. As Table II shows, our estimate was excellent in one case, fair in another, and somewhat off in two cases.

Table II. Determination of Grating Period and Effective Index

Run #	$n_{effective}$ (Calculated)	Period of Grating, P (Å)	Lasing Wavelength, λ (Å)	$n_{effective}$ (Measured) λ/P	n_e Calc. $- n_e$ Meas.	Threshold Current (mA)
1107	3.350	3970	13,290	3.348	0.002	60
1112	3.300	3900	12,750	3.270	0.030	160
1113	3.336	3870	12,800	3.307	0.029	400
1117	3.378	3900	13,150	3.372	0.006	110

VII. GRATING CONFIGURATION

The general objective in designing the grating shape to achieve optimum operation is to obtain the largest possible coupling coefficient, k, which is a measure of the backscattering, i.e., feedback by the grating. A large value for k is advantageous as the device will be strongly locked into the grating mode and will be less likely to lase on a Fabry-Perot mode. The parameter of interest is the product of the coupling coefficient and the laser cavity length L. It has been shown [10] that only if kL has values in the vicinity of 1 will the power density in the cavity be reasonably flat from end to end. For values far from unity, all the power is concentrated at the ends ($kL << 1$) or in the middle ($kL >> 1$). Distorted power distributions are incompatible with normal performance. This is because they leave a lot of unused gain in the device, which can then support another mode. Another constraint arises from the need to keep the device length short to maintain reasonably low threshold currents. To obtain $kL = 1$ for short lasers, k has to be large, say 50 to 100 cm^{-1}.

The question then arises as to the best grating shape for achieving this high value. There are several new constraints: (a) the danger of excessive meltback of the grating during the overgrowth, (b) the difficulty of fabricating the desired grating shape, (c) the facilities available for the fabrication, i.e., electron beam writing, optical holography, dry or wet chemical etching, etc.

The coupling coefficient depends on the thickness of the waveguide layer, the width and depth of the corrugation, the Fourier component of the grating profile, the dielectric step, etc. The most important factor is the grating shape, since some shapes favor first-order diffraction, and others higher-order diffractions. Figure 27 shows the coupling coefficient for two gratings, a rectangular one, which requires both even and odd Fourier components for its decomposition, and a triangular one, for which the even Fourier components vanish. The triangular grating has a much lower coupling coefficient for second-order gratings, but the rectangular grating has about the same coupling coefficient for both first and second-order gratings.

There is no general agreement about the optimum grating shape for second-order gratings, no doubt because of the considerable effort required to make accurate coupling coefficient calculations. One group prefers a rectangu-

lar, narrow, and very deep grating [19], whereas another claims that a trapezoidal shape is the one giving the highest coupling coefficient [3].

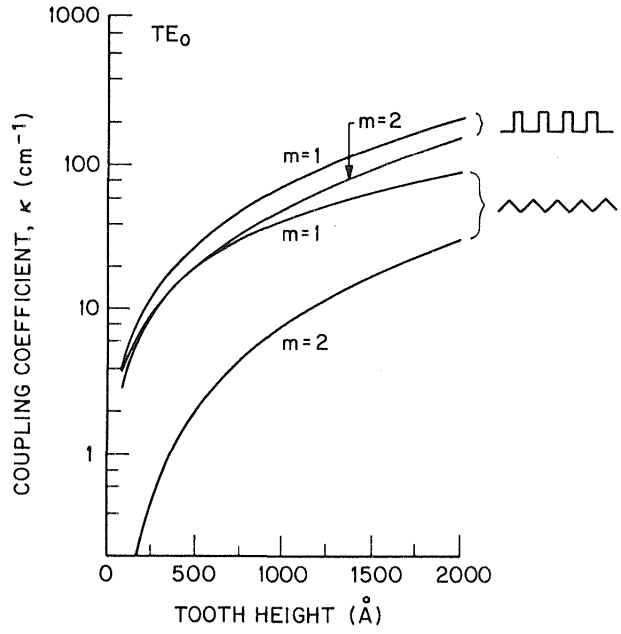

Figure 27. Coupling coefficient as reported by Streifer et al. for square and sawtooth gratings. The square grating has about the same coupling coefficient for the first- and second-order gratings, while the sawtooth grating is much poorer for second-order gratings.

The following observations pertain to the V-groove grating used for most devices in this research. Figure 28 presents the progression of shapes obtained by etching a suitably coated wafer oriented with the grooves in the [0,1̲,1] direction. Etching progresses both downward and sideways and continues until a triangular shape is reached, at which point the etching stops. For the V groove, the included angle is 72°, and in the case of a 4000-Å period, the tooth height will be 2752 Å, which will be reached automatically, providing etching is carried out long enough. However, one cannot take advantage of this fact in making second-order gratings since the grating coupling coefficient for a second-order symmetric-triangle grating is small [18]. Rather, the etching must be stopped before the maximum diffracted signal is obtained to achieve a shape similar to that shown in Figs. 28b or 28c, which were the grating profiles used in this program.

There appears to be some advantage in fabricating first-order gratings, with the fully developed tooth height of a triangular grating being 1376 Å. In

addition, with first-order gratings, a method for introducing a phase shift must be included since the radiation loss, which is the main mechanism that promotes the single-line emission with second-order gratings, is absent. However, the advantage of the first-order grating is that it provides high coupling coefficients, and the grating etch is self-limiting and therefore reproducible.

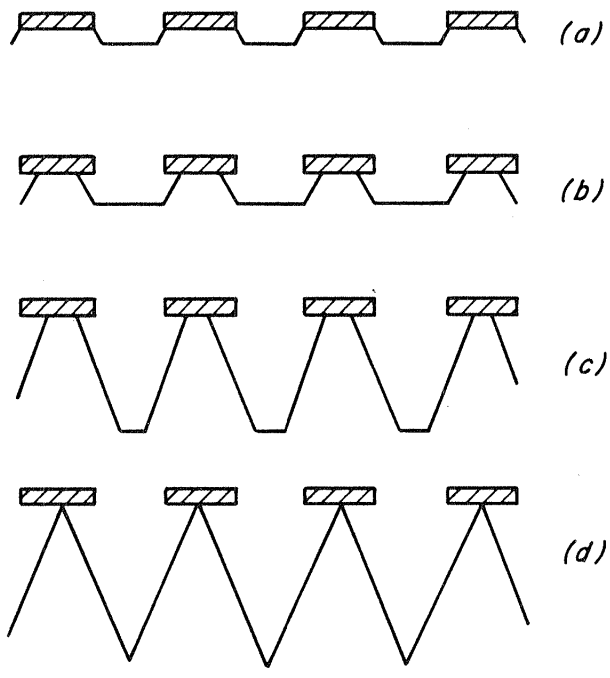

Figure 28. Etching progression in the sawtooth grating.

VIII. FABRICATION OF GRATINGS IN InP AND InGaAsP

Two schemes of fabricating the gratings were tried during this program. In the first, we produced a grating in a metal photomask and then, using conventional aligners, transferred this grating into photoresist deposited on the wafer. This approach was chosen because the method had been demonstrated by RCA's Zurich Research Laboratory to work for periods as low as 3800 Å, and because their technology could be used in this process. However, this scheme was abandoned because of the awkwardness associated with the two-step procedure of making a mask before transferring the grating into the material. This was especially a problem because each wafer requires a different grating period. Thus, while this method eliminates the need for a holographic exposure facility, it is difficult to use for adapting the grating to the bandgap of the active layer on different wafers. This is due to the variability in the bandgaps obtained from a series of wafers.

Therefore, the research concentrated on constructing a new holographic exposure system built specifically for grating fabrication. The process of exposing the photoresist by holography is based on employing two interfering light beams (Fig. 29) that produce a diffraction pattern in the photoresist; when developed, this pattern becomes the mask for the transfer of the grating into the semiconductor material. This transfer was carried out exclusively by wet chemical etching.

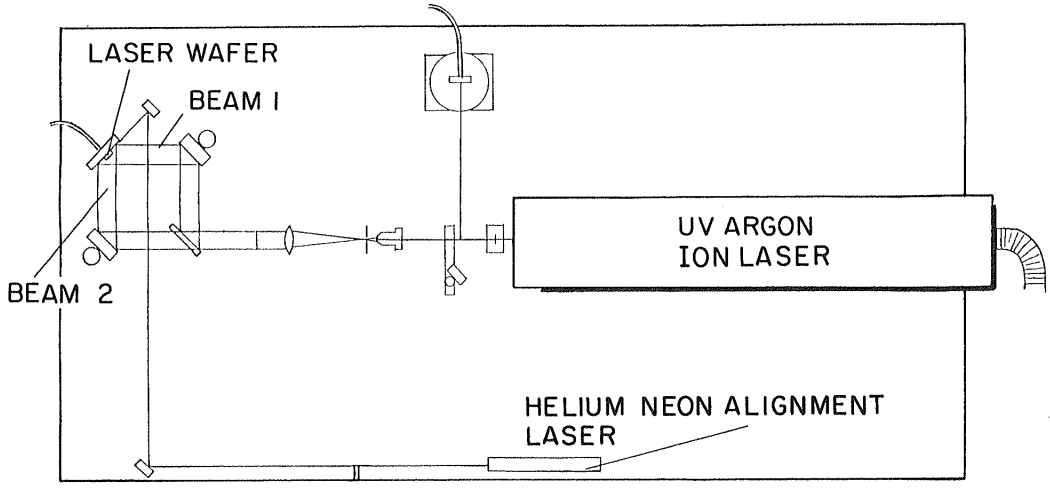

Figure 29. Schematic diagram of the arrangement generating the diffraction pattern used to fabricate the grating.

Although any of several chemical solutions could be used to etch the gratings, it has been difficult to find systems that etch InGaAsP at a rate fast enough to prevent photoresist deterioration during the etch. Various formulations of H_2SO_4:H_2O_2:H_2O attack InGaAsP, but the usual photoresist must be baked carefully if it is to survive the etch. Another approach was to coat the wafer with SiO_2 and then apply the photoresist. The expectation was that the grating could be transferred quite rapidly into the oxide by the use of buffered HF, and that the oxide mask would be resistant enough to allow etching of the grating with conventional etches. However, it was found that the inclusion of the SiO_2 film altered the photoresist exposure process to such an extent that no grating pattern was obtained.

In retrospect this might have been expected, since the electric field maximum at the photoresist-to-semiconductor interface is transferred to the semiconductor-to-oxide interface, where it is much less effective in causing photoresist exposure. It appears that profound modifications of the exposure can be produced by an appropriate choice of oxide film thickness, and it seems entirely feasible to work out a suitable process based on the use of a dielectric layer. However, the discovery of a new etch formulation [15] that showed exceedingly rapid etching and minimal photoresist attack rendered these investigations unnecessary. This etch is a mixture of bromine, phosphoric acid, and water in the ratio of 1:1:15.

Depending on the crystal orientation, two distinctly different grating profiles can be obtained. The first, with the grooves aligned in the [0,1,1] direction (dovetail grating), is shown in Fig. 30, and the second, with the grooves oriented in the [0,$\underline{1}$,1,] direction (V-groove grating), in Fig. 31.

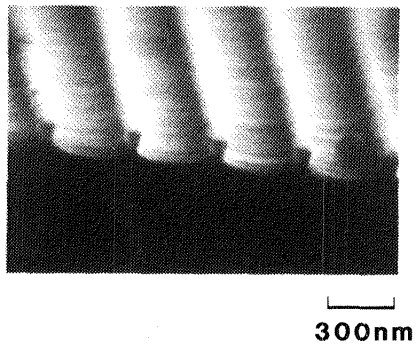

Figure 30. SEM photograph of etched dovetail grating.

Detailed calculations of the effect of these two profiles on laser characteristics are lacking, but certain general observations can be made. The grating of Fig. 30 has a more angular and projecting structure, suggesting a higher scattering power than that for the V-groove shape. This would make it more desirable for the laser, as it would yield a higher coupling coefficient.

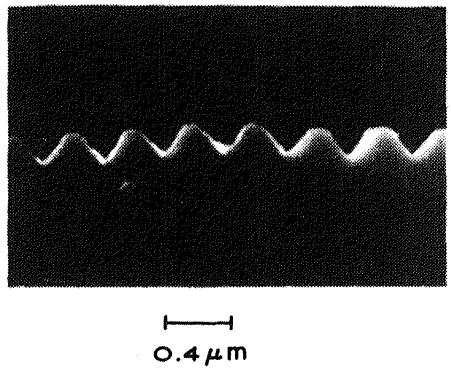

Figure 31. SEM photograph of etched V-groove grating.

However, the growth-induced erosion of this shape can be more severe, and the danger exists of the grating being undercut and completely removed by the effect of the melt applied to it during the regrowth step. In several instances, when the grating was formed in the dovetail direction, no grating was observable after regrowth and subsequent etching down to the surface on which the grating had been formed. Principally because it yielded the best preserved grating shape during the regrowth step, we restricted most of our work to the structure in Fig. 31.

After the grating period is determined, the wafer containing the active and waveguide layers is coated with photoresist and exposed to the interference pattern generated from the beam of an argon laser emitting in the UV at 3511 Å. The photoresist is then baked, developed, and postbaked, at which point it is ready for etching.

During the etch process, the grating efficiency is monitored with a HeNe laser. This is done by illuminating the wafer surface with the HeNe laser and measuring the intensity of the first-order diffracted beam (i.e., used as a standard bulk diffraction grating). The wafer is briefly immersed in the etching solution, typically for 10 seconds, and removed from the solution; then the diffracted beam intensity is measured. To ensure that the measured diffraction efficiency is typi-

cal of the wafer, the beam is scanned around the sample. This process continues until the diffracted beam intensity reaches a value that has been correlated with the desired grating shape in previous experiments.

The next three figures (Figs. 32 to 34) are SEM photographs of several gratings, for which the corresponding diffracted beam intensity (as described above) is given in Table III. The diffraction efficiency, defined as the ratio of the power diffracted into the first-order to the incident power, increases as the amplitude increases. Most of the gratings fabricated here had a shape between those of Figs. 32 and 33, and a diffraction efficiency between 1.5% and 5%. However, a single measurement of the diffracted beam intensity is not sufficient to define both the grating shape and depth. Errors are introduced by slight variations in the photoresist and exposure, which affects both the diffracted beam intensity and the actual etching profile.

Unfortunately, because the measured first-order diffraction efficiency and the coupling coefficient depend in different ways on the grating shape and depth, one cannot correlate these two quantities in a simple manner. A rapid, nondestructive method of assessing both the grating shape during the etch process would therefore be very desirable. Such a method might be based on ellipsometric measurements.

The ridge-guide laser structure requires that a layer of InP be regrown over the grating surface. Regrowth involves cleaning, heating, and a regrowth step in the course of which a melt of In is brought into contact with the grating surface. Because all of these steps are deleterious to the grating, precautions need to be taken to avoid excessive deterioration. Normally, these precautionary steps are taken: the grating is cleaned in solvents, water, HF, and H_2SO_4. These agents do not significantly dissolve either InP or InGaAsP. The most reactive of them is H_2SO_4, which attacks InP at a rate of 60 Å/min.

Table III. Diffracted Beam Efficiency vs Grating Shape

Sample		Efficiency (%) (As etched)	Efficiency (%) (PR stripped)	SEM shown in Fig. No.
(1101)	A	1.35	0.8	32
(QC-42)	B	6.00	7.0	33
(15-13)	C	15.00	12.5	34

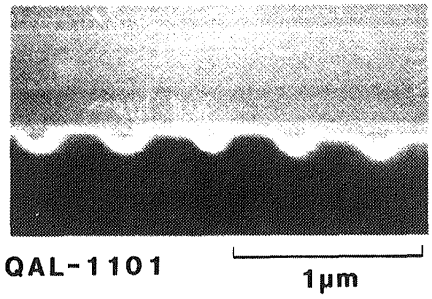

Figure 32. SEM photograph of grating A for Table III.

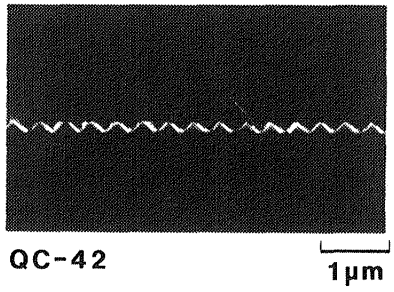

Figure 33. SEM photograph of grating B for Table III.

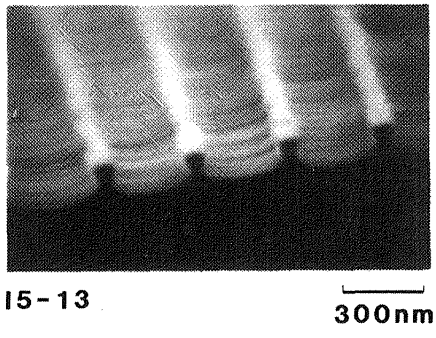

Figure 34. SEM photograph of grating C for Table III.

The next precaution consists in reducing the time the wafer remains at high temperature, and reducing the growth temperature to 590°C. Finally, the grating is covered with a wafer of GaAsP to protect the surface during the pre-heating cycle in the furnace. It appears that this causes some As to be deposited on the wafer surface, thereby reducing grating deterioration by reducing

meltback. The effect of As is quite significant, and is easily observed when the surface of a freshly grown InP layer is compared with that of a freshly grown InGaAsP layer.

In general, one must protect against erosion due to the high temperature, and against meltback, and As seems to be beneficial in both cases. Figure 35 demonstrates the appearance of a grating just after being chemically etched (Figs. 35a and b) and, again, after growth and subsequent removal of the grown layer by selective etching (Figs. 35c and d). It is apparent that the grating (in the V-groove direction in this case) is preserved after regrowth and etching of the InP p-cladding layer.

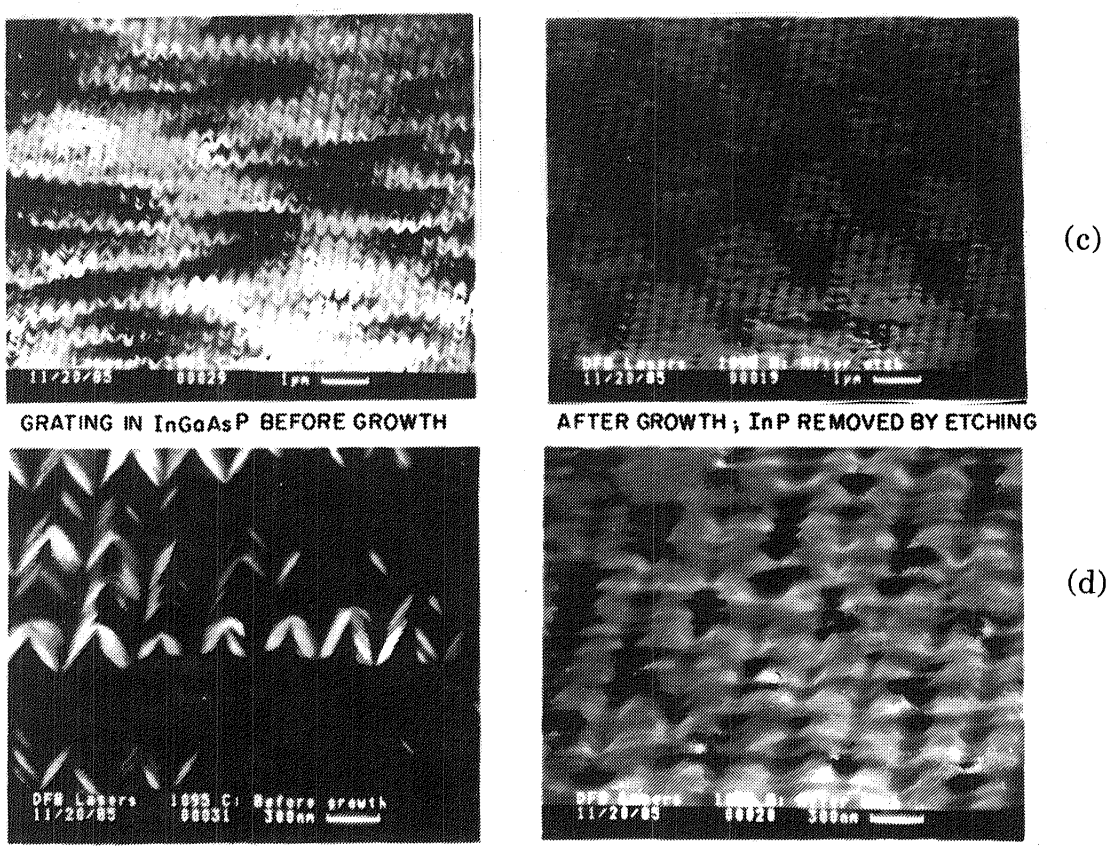

Figure 35 Demonstration of growth over the grating. (a) and (b) show the grating appearance immediately after etching (at two different magnifications); (c) and (d) after overgrowth and subsequent removal of the overgrowth.

IX. FABRICATION OF RIDGE-GUIDE LASERS

The fabrication process for the ridge-guide DFB laser is depicted schematically in Figs. 36 and 37. This involves two growth steps, two etch steps, and the necessary photolithography. The first growth consists of four epitaxial layers on a sulfur-doped (100) InP substrate. These layers are an n-type InP buffer layer, an InGaAsP active layer, an InP carrier confinement layer, and an InGaAsP waveguide layer. Table IV shows the thicknesses, doping, photoluminescence wavelength, and effective index of these layers. A grating is etched into the waveguide layer with a process described in the section on grating fabrication.

Overgrowth continues with two more layers: the InP p-cladding over the grating and an InGaAsP cap layer. After overgrowth, two 10-μm wide channels, 5 μm apart, are defined in the photoresist perpendicular to the grating. These are etched, defining the 5-μm wide ridge. After etching in HCl, the ridge is 5-μm wide on top, narrowing to less than 3.5 μm where it meets the waveguide layer. The crystalline orientation of the substrate and the etchant used are selected to make the bottom of the ridge narrower than the top. This is done to get a wide contact stripe for low contact resistance at the same time as getting good single-mode optical confinement under the narrow bottom of the ridge.

Once the ridges are formed, SiO_2 is deposited, the contact stripe is opened on the ridge; and the wafer is metallized and thinned. Finished devices are then mounted p-side down on copper heatsinks by means of In solder. A gold lead is attached to the n-side also with In solder.

Table IV. Layer Parameters used in Ridge-Guide DFB Lasers

Layer	Thickness (μm)	Doping	PL-Wavelength (μm)		Index
n Cladding	2 - 3	n 2E18	0.92	InP	3.20
Active	1.1	undoped	1.3	InGaAsP	3.49
Carrier Conf.	400Å	p 1E17	0.92	InP	3.20
Waveguide	0.12-0.16	p 3E17	1.1	InGaAsP	3.33
p Cladding	1.5 - 2	p 7E17	0.92	InP	3.20
Cap	0.5	p 2E-18	1.6	InGaAsP	-

One important step in the processing is the deposition of the oxide on which the metal is to be evaporated (second step in Fig. 37). To reduce leakage from the sidewalls at the outside edge of the channels (away from the ridge), it is desirable to coat the vertical ridge walls with a dielectric film. To accomplish this, we have used plasma chemical vapor deposition. As an example of the result of this procedure, Fig. 38 shows the side walls of the channel effectively coated with dielectric.

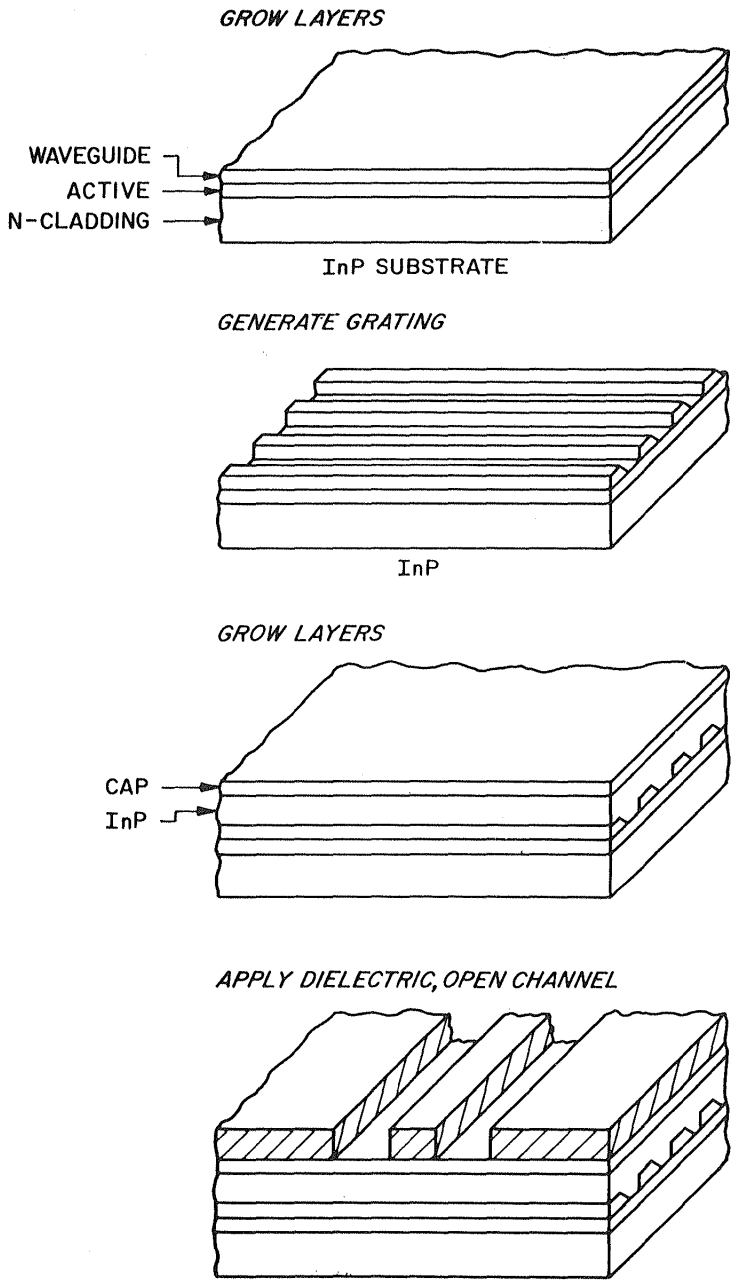

Figure 36. Processing steps used in fabricating ridge-guide lasers.

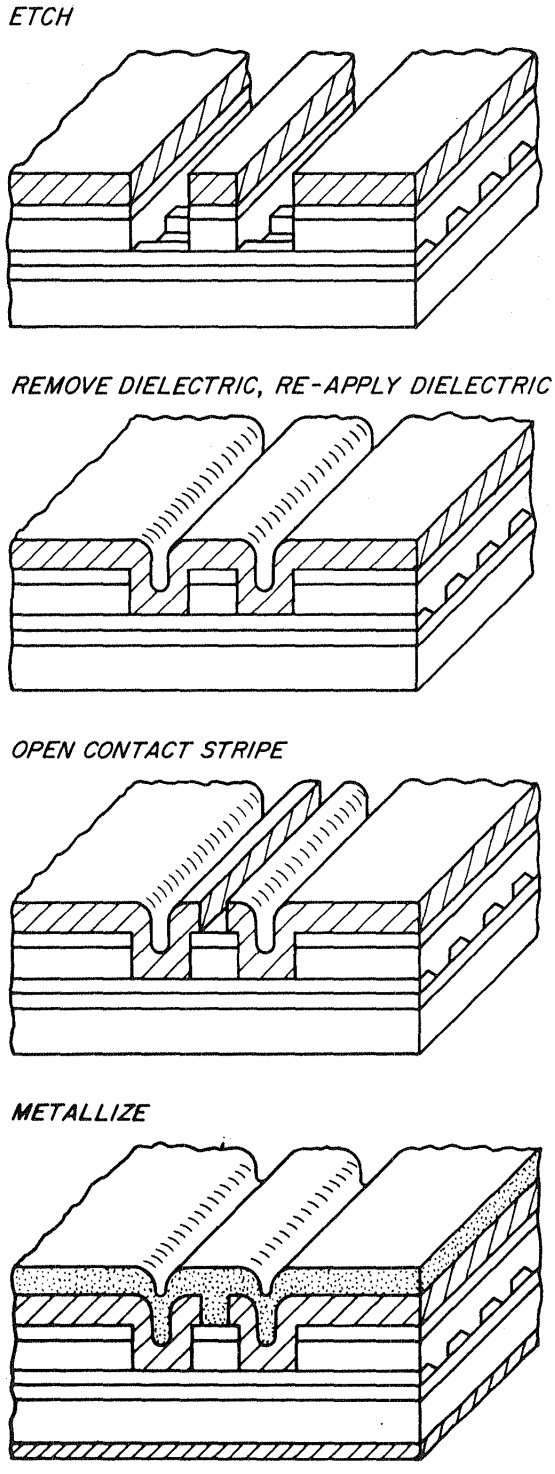

Figure 37. Further processing steps in ridge-guide fabrication.

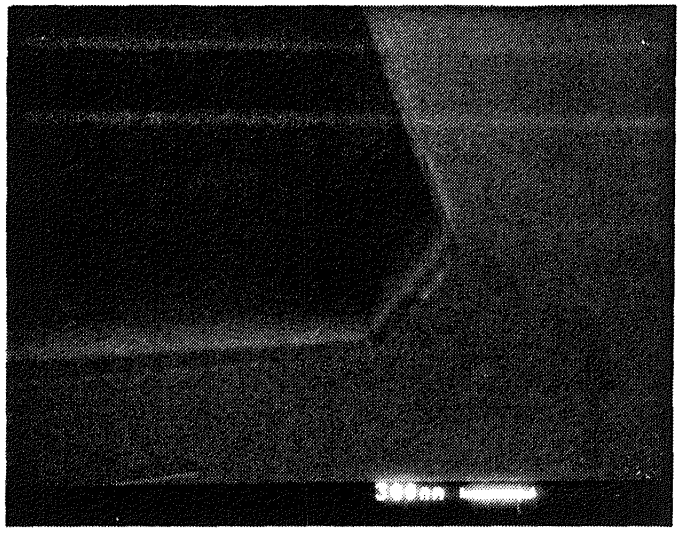

Figure 38. Conformal dielectric deposition on sides of the ridge-guide.

X. CADMIUM DIFFUSION

All material growth in this project employed Zn as the p-type dopant. However, there are certain disadvantages to using Zn, most significantly that it diffuses during growth, so that the p-n junction is usually displaced from its original position. Sometimes this proves to be an advantage as one can shift the p-n junction away from the metallurgical boundary, but it also imposes a severe limit on the amount of Zn one can incorporate into the structure.

Thus, the maximum Zn doping is restricted to the $10^{17}/cm^3$ regime, which manifests itself in larger than desired contact resistances, and lower than desired p-type doping. In the case of contact resistance, in which high surface doping is required to reduce the resistance, the problem is that Zn can be diffused to a high surface concentration, but it is not possible to keep it within a shallow region near the surface. Diffusion conditions that keep the Zn shallow lead to low surface concentrations.

Cadmium is an alternative to Zn, and indeed its diffusion rate is much smaller than Zn, although its higher vapor pressure creates new problems. Some experiments employing Cd as a possible dopant to be introduced by diffusion into the surface for the purpose of generating highly doped shallow regions suitable for contact metallization were made during this project. The existing literature on Cd diffusion deals mostly with diffusions of long duration and deep penetration (on the order of several μm) [7,2] although there is one paper [4] dealing with short diffusions of Zn and Cd. However, this only considers elemental Cd, and no studies have been made of diffusions using Cd with either P or In included in the ampoule, a method shown to yield greatly reduced diffusion depths [5] using 4-h diffusion times.

In this work, short duration diffusions into InP were examined, using Cd and Cd with either P or In as the diffusion source. Diffusions were carried out into Sn-doped InP with a carrier concentration of 8.5×10^{17}, and into Fe- doped semi-insulating InP. Samples were sealed into quartz ampoules of approximately 0.6 cm^{-3} volume, containing one of three different charges: (a) 3-mg Cd, (b) 3-mg Cd and 10-mg red P, and (c) 3-mg Cd and 10-mg In. Diffusions were carried out for 15 min. at 625°C .

In some cases, diffusions were also made into InGaAsP layers, which were then processed for contact resistance measurements using a method described

previously [12]. After diffusion, the samples were cleaved, stained in ferricyanide etch, and the position of lines or changes in contrast measured by microscopy. In the case of doped samples, this was taken to be the position where the diffused concentration equals the substrate n-type doping; for the semi-insulating samples this was taken to be the position where the diffusion front suffers a change in slope; and for the deep line, where the concentration drops below 1 x 10^{15} cm^{-3} [6]. The results of these experiments are given in Table V.

Samples of the diffused semi-insulating InP were also submitted to Charles Evans Associates for SIMS depth profiles. Their results are presented in Figs. 39, 40, and 41. Also shown in these figures are the points obtained from the junction depth for doped samples (labeled A), and from visible features as revealed by staining in semi-insulating samples (labeled B).

Table V. Depth of Features Shown by Chemical Staining

Ampoule Charge	Test Sample	Depth (μm)
Cd	InP:Sn	1.2
Cd/In	InP:Sn	0.3
Cd/P	InP:Sn	0.3
Cd	InP:Fe	2.9 & 5.6
Cd/In	InP:Fe	1.7
Cd/P	InP:Fe	0.7

The SIMS data for the Cd-only and the Cd + In diffusions show high surface concentrations. It is not clear whether these are real, or whether they are a result of a surface deposit of metallic Cd. Considering the sharp break in the curve, it is likely that the high values for the Cd-only diffusion are due to a surface film. On the other hand, the Cd + In diffusion data indicate what appears to be a real, shallow, high-concentration surface layer. A discrepancy exists between the junction depth and the SIMS data in the case of the Cd-only diffusion (point A in Fig. 39).

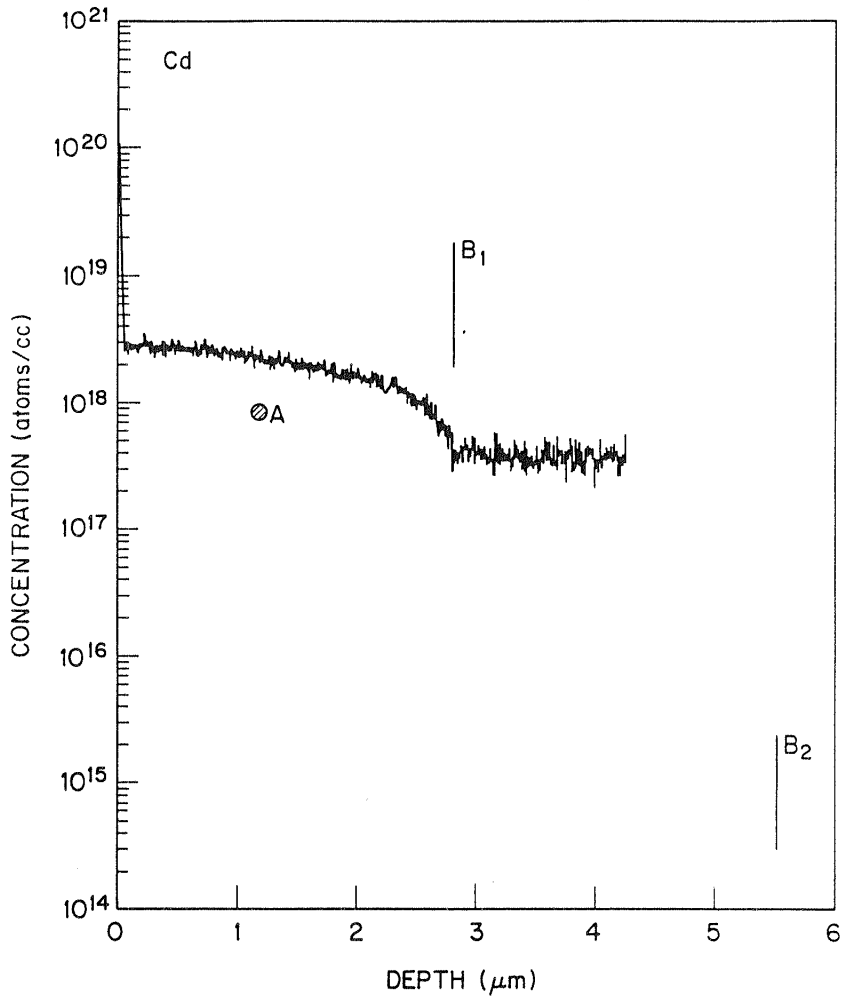

Figure 39. SIMS depth profile of Cd diffusion in semi-insulating InP (courtesy of Charles Evans Associates). Point A is location of the junction line in simultaneous diffusion into n-type InP; and B1 and B2 are locations of lines revealed in staining cross-sections of semi-insulating material.

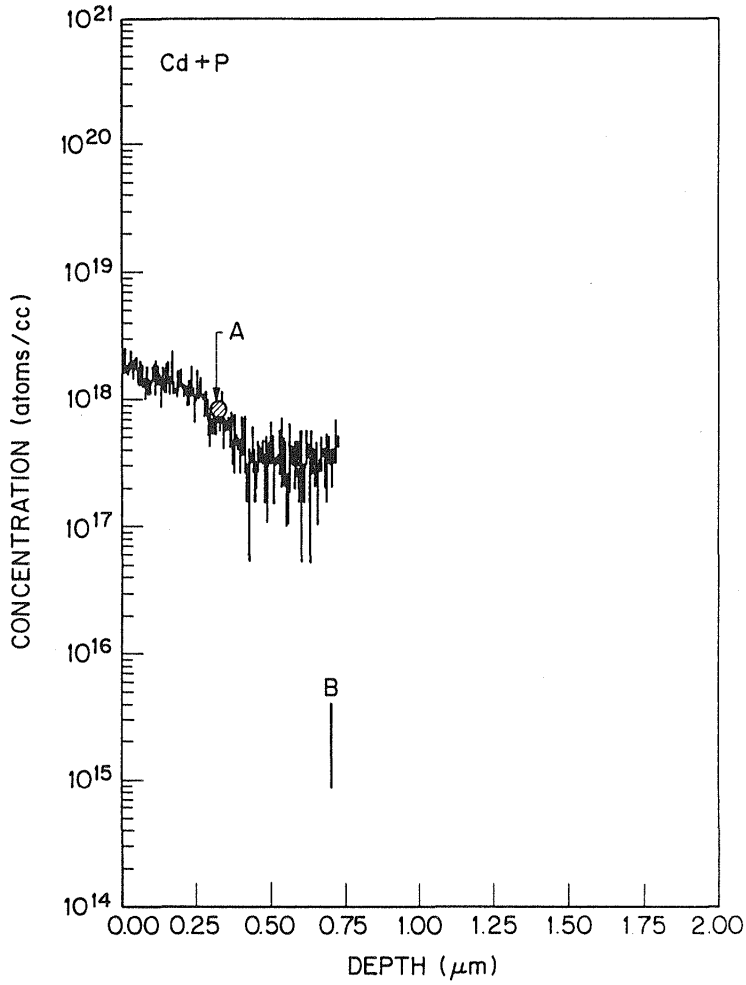

Figure 40. Same information as in Fig. 39 for diffusion of Cd in the presence of P.

However, the accuracy of the SIMS concentrations is stated to be within a factor of 2, which is sufficient to remove most of the difference. Furthermore, one must consider the influence of the doping on the diffusion process itself [11], which yields higher diffused concentrations in the case of undoped samples than in the case of n-doped samples processed under identical conditions. The SIMS data and our optical depth measurements were combined into an estimate concentration profile for the three types of diffusions carried out during this work (Figs. 42, 43, and 44).

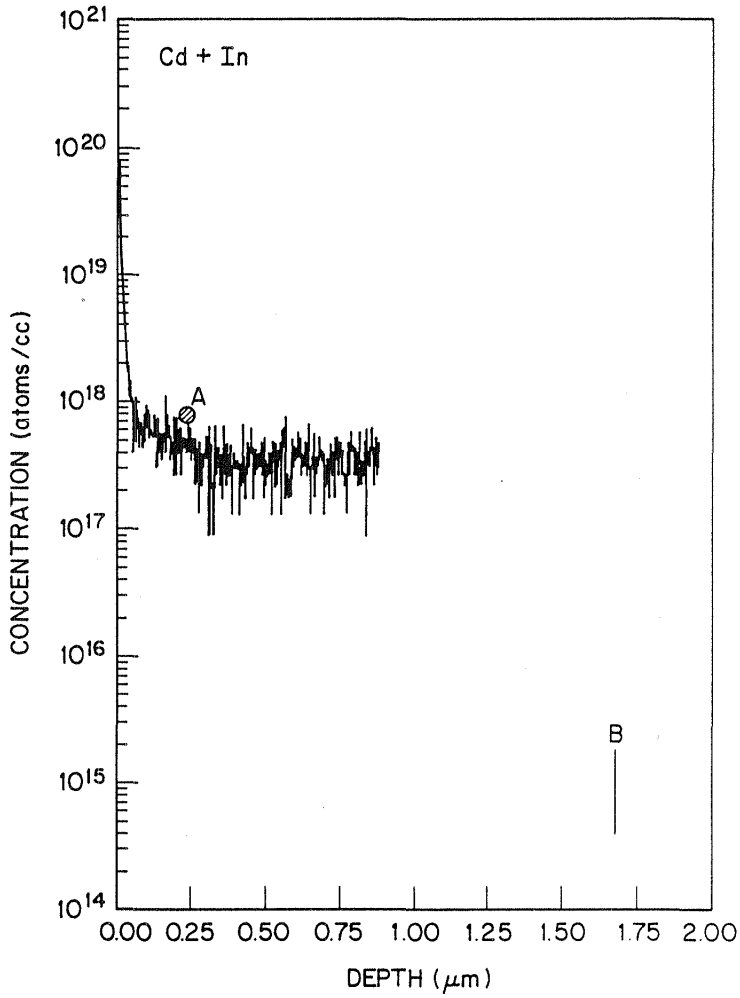

Figure 41. Same information as in Fig. 39 for diffusion of Cd in the presence of In.

In selecting samples for contact resistance measurements, the Cd-only diffusion was rejected because of its large penetration depth. The remaining two cases were examined by making contact resistance measurements on layers of InGaAsP grown on InP, which were introduced into the ampoule simultaneously with the samples discussed earlier. The results are given in Table VI.

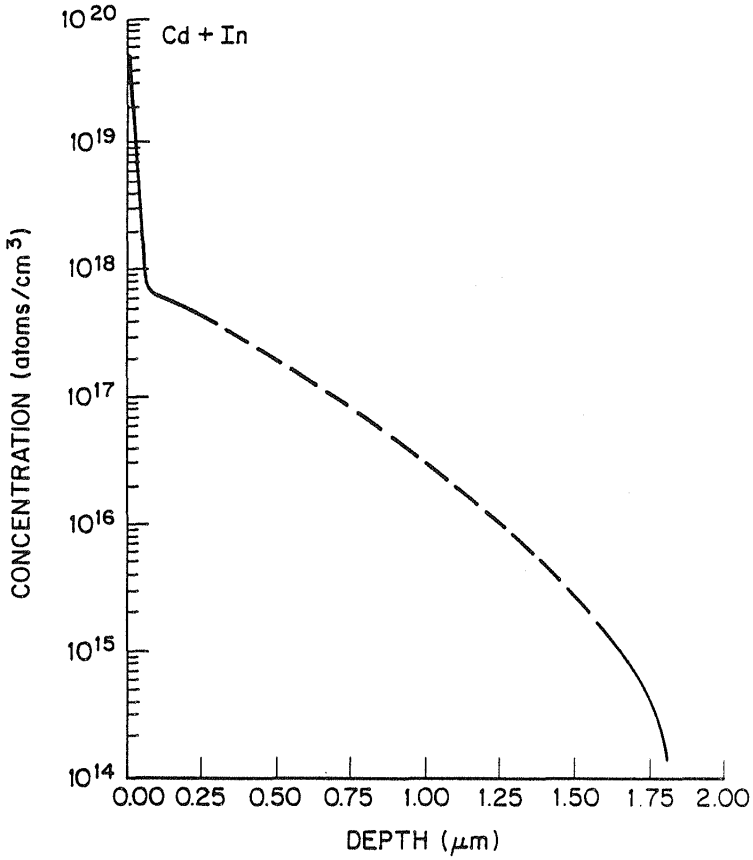

Figure 42. Estimated diffusion profile for Cd + In InP.

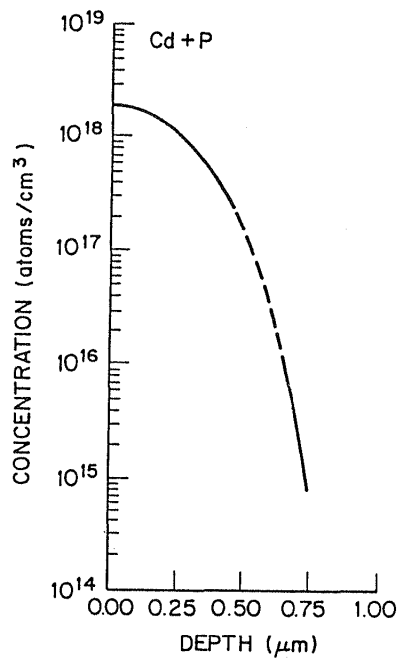

Figure 43. Estimated diffusion profile for Cd and P in InP.

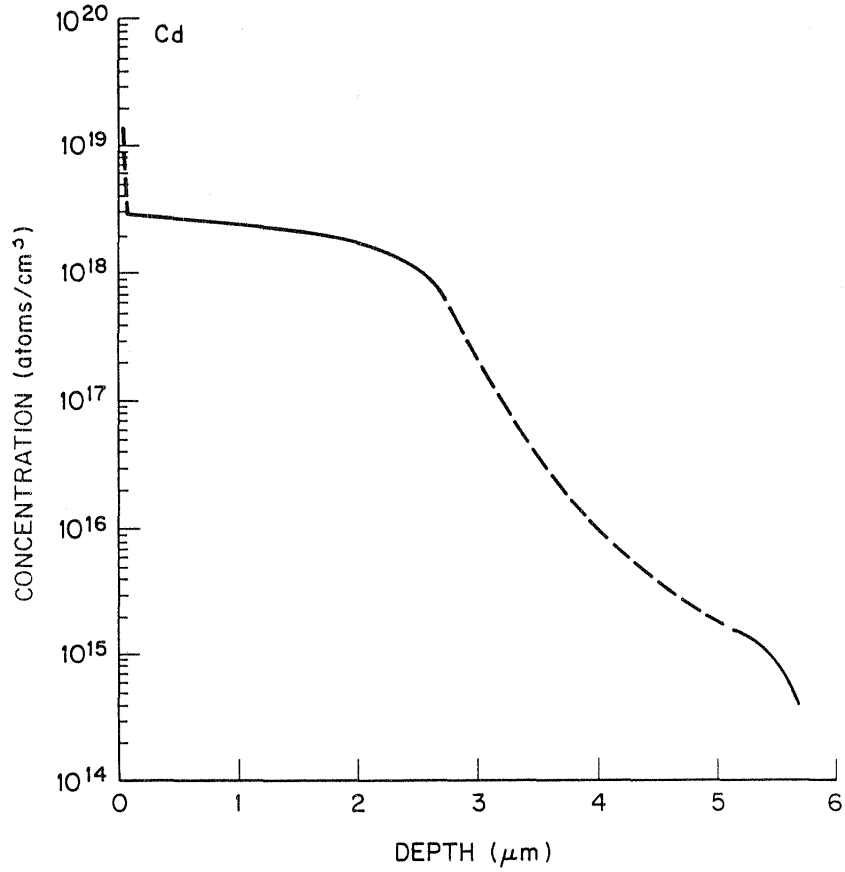

Figure 44. Estimated diffusion profile for Cd in InP.

Table VI. Contact Resistance of Ti/Pt/Au Metallization on Diffused InGaAsP

Diffusion Charge	Sample Bandgap Wavelength μm	Doping	Specific Contact Resistance (Ω-cm^2)
Cd + P	1.53 μm	undoped	1.9×10^{-5}
Cd + In	1.6 μm	Zn doped	1×10^{-3}

It is apparent that only the Cd + P diffusion yields an acceptable contact resistance value. The failure in the Cd + In case may be caused by the removal of some surface material during contact preparation. Thus, the loss of 500 Å is sufficient to drop the carrier concentration to the 7×10^{17} cm^{-3} value. A better clean-up process before metal evaporation may lead to significant improvements using Cd + In diffusions.

XII. DEVICE RESULTS

A number of wafers were grown and fabricated into ridge-guide DFB lasers during this program. These devices, the structure of which is described ealier in this report, were mounted p-side down onto copper heat sinks using In solder. The laser facets were not coated. It is possible to classify the results obtained according to the spectra produced by these devices as follows:

(a) Lasers showing no evidence of spectral selection
(b) Lasers showing double line emission
(c) Lasers showing other spectral properties
(d) Lasers showing single line emission

Type (a) lasers have uninteresting spectra, reminiscent of lasers without a grating. Probably, the grating is missing or the coupling is insufficient because of excess distance between the grating and the active layer.

Type (b) lasers behave as expected from the standard model of the DFB laser, i.e., the excitation of two lines symmetrically disposed around the Bragg wavelength [10]. Figure 45 illustrates examples of such spectra.

From the two-line DFB spectra shown in Fig. 45, an estimate of the grating coupling coefficient can be made. In a simple model, the separation between the two modes is equal to the grating stop band, which is directly related to the product of the grating coupling coefficient (k) and device length (L). (The relation between the mode spacing and stop band really only holds when any facet effects are negligible, which is difficult to verify. Furthermore, an accurate calculation would require that we meaure the mode spacing at threshold.) From Fig. 45, if we take a mode spacing of 27 Å and a device length of 200 μm, we find that kL=3 or $k=150cm^{-1}$, which is larger than desired. For most of the successful devices fabricated, however we estimate that kL<1, which was only marginally strong enough. For these small coupling coefficients, the mode spacing is only slightly perturbed from the Fabry-Perot spacing, making an accurate determination difficult. As a result, we were not able to make a good estimate of kL for the devices that showed the best DFB characteristics.

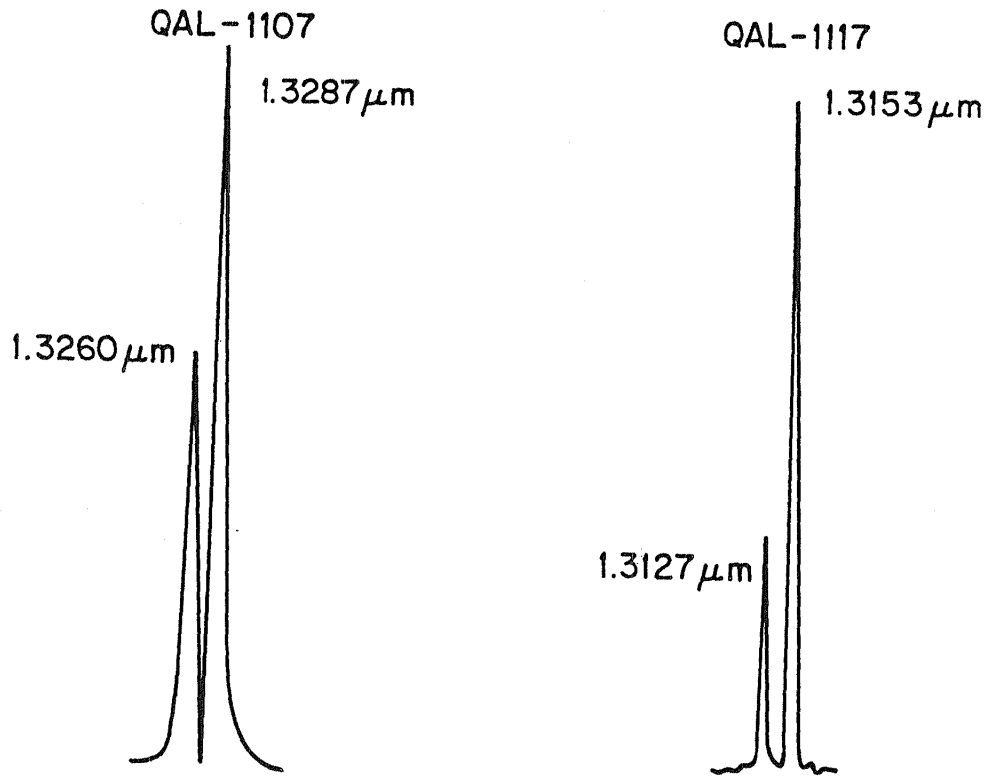

Figure 45. Examples of two line spectra measured on devices (from wafers #QAL-1107 and #QAL-1117) lacking significant discrimination between the two allowed modes.

An interesting spectrum of type (c) is shown in Fig. 46; the device oscillates in a single spectral mode at lower current drive, and then switches to two symmetrically disposed lines at higher drives. This suggests that the single-line emission is the gap mode [8], and the two lines are the pair of allowed grating modes.

Type (d) devices are the successful lasers. For the best wafers, they represent about 10% of the devices tested. Figure 47 shows power vs current curves for one of these lasers, at a series of temperatures. The lowest threshold is 50 mA at a temperature of 15°C, which rises to 60 mA at 25°C. A power output of 7 mW is shown, and it is expected that these devices will deliver at least 10 mW.

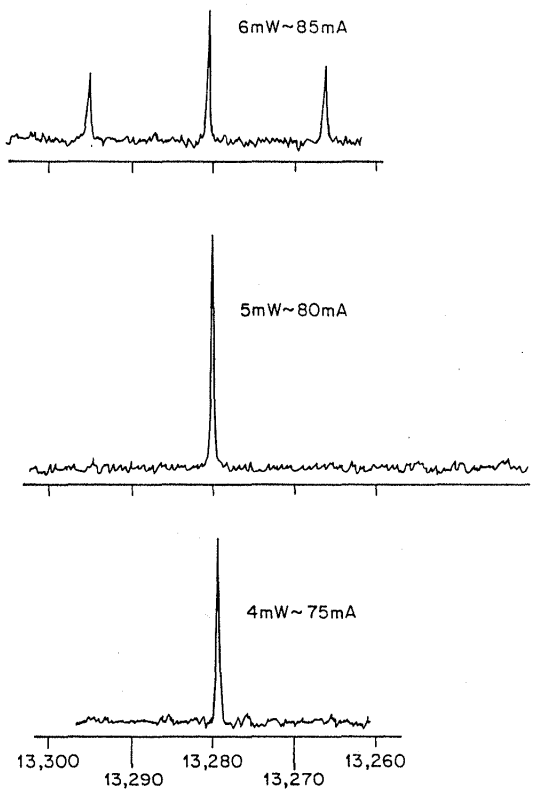

Figure 46. Single-line spectrum at the gap-mode, and the two symmetric DFB lines arising at higher drive (wafer #QAL-1107).

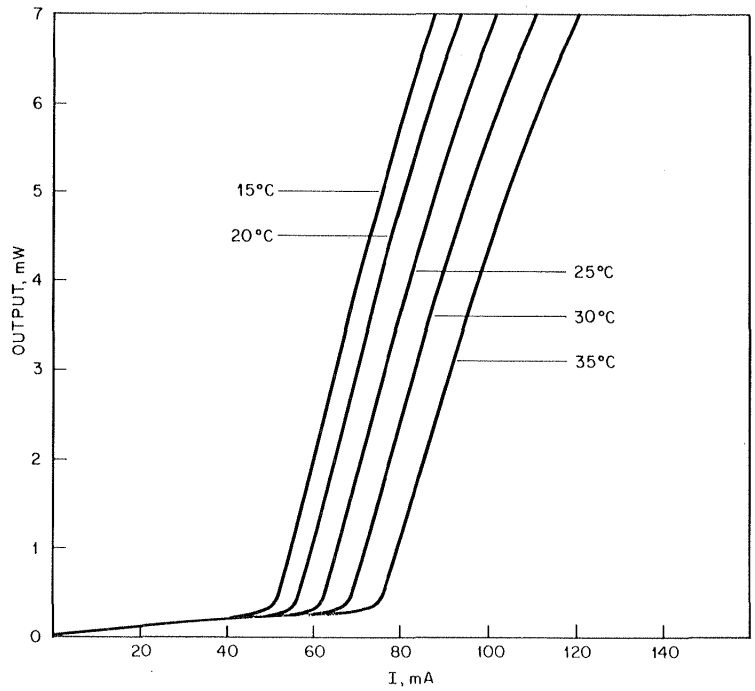

Figure 47. P-I characteristics of ridge-guide DFB lasers developed under this contract (wafer #QAL-1107).

Figure 48 presents spectra at two different temperatures for a series of output power levels. The small shift seen in these curves is caused by the effect of self-heating on the refractive index. Figure 49 displays the spectrum for a series of temperatures and output levels. The temperature-dependent wavelength shift here includes some contribution from selfheating, especially at currents above 100 mA.

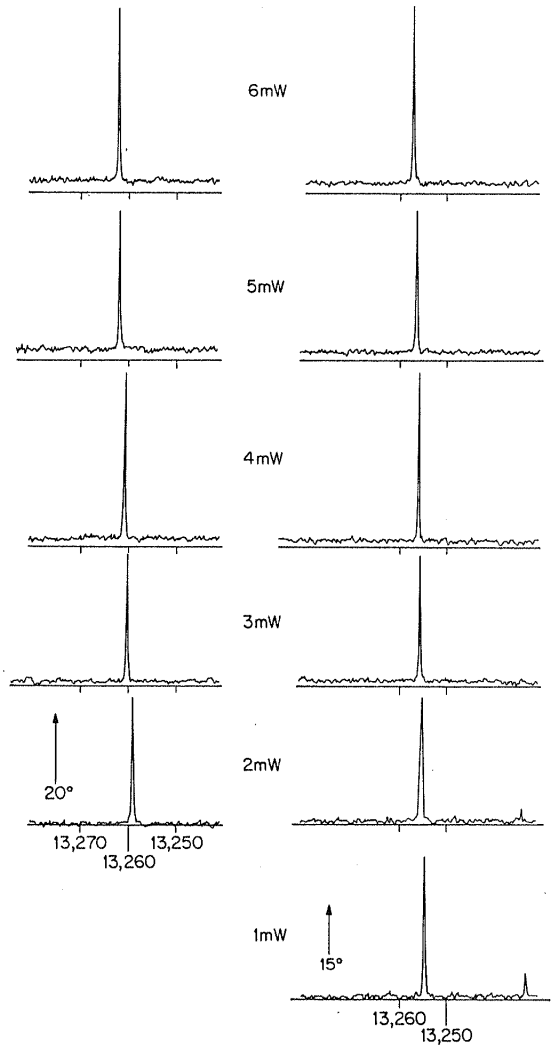

Figure 48. Spectrum of a ridge-guide DFB laser developed during this contract (wafer #QAL-1107). The change of wavelength with increasing power is shown at two different heat sink temperatures.

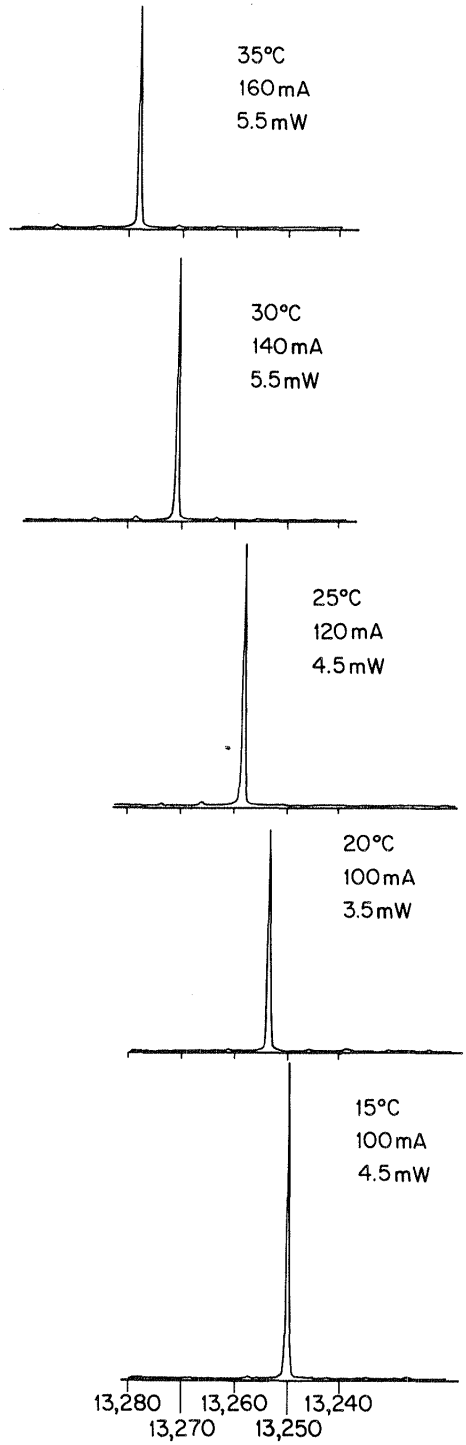

Figure 49. Emission spectrum of a DFB laser fabricated during this contract as a function of heat sink temperature (wafer #QAL-1107).

The best test of a DFB laser is to measure the output wavelength as a function of temperature at a constant drive current. For a DFB laser, the primary

mechanism responsible for temperature-dependent wavelength changes is the change in index of refraction with temperature, which is about one part in 10^4/°C. The change in the grating period caused by the thermal expansion coefficient is more than an order of magnitude smaller and therefore negligible. In a DFB laser, the lasing wavelength is locked by the Bragg wavelength of the grating, which is given by

$$\lambda_B = \frac{2n_{eff}P}{m} \tag{11}$$

where n_{eff} is the effective index, and m and P are the grating order and period, respectively. Differentiating with respect to temperature yields

$$\frac{d\lambda_B}{dt} = \frac{1}{n_g} \lambda_B \frac{\partial n_{eff}}{\partial T} \tag{12}$$

where n_g, the "group" index, is given by

$$n_g = \left(n_{eff} - \lambda \frac{\partial n_{eff}}{\partial \lambda} \right) \tag{13}$$

and dP/dT, is assumed small. For our DFB lasers operating at 1.3 μm, n_g is approximately 4 (determined from the Fabry-Perot mode spacing), dn/dT is about 3×10^{-4}, and we find that the wavelength change with temperature should be about 1 Å/°C.

One finds that change in wavelength of a Fabry-Perot mode with temperature is also 1 Å/°C. However, in a Fabry-Perot laser mode hopping will occur as the peak of the gain curve changes with temperature. Since the gain curve shifts at a rate of about 2.5 Å/°C, one would expect to see a mode hop in a 250-μm-long Fabry-Perot laser after a temperature shift of about 7°C.

Plotted in Fig. 50 is the change in wavelength of a DFB laser as the heat sink temperature is increased from 16°C to 28°C. By fitting the data to a straight line, we find the wavelength tunes at 0.8 Å/°C, which is consistent with our estimate above. Furthermore, we see that there were no mode hops in this 12°C temperature range, which was limited by the thermoelectric cooler used.

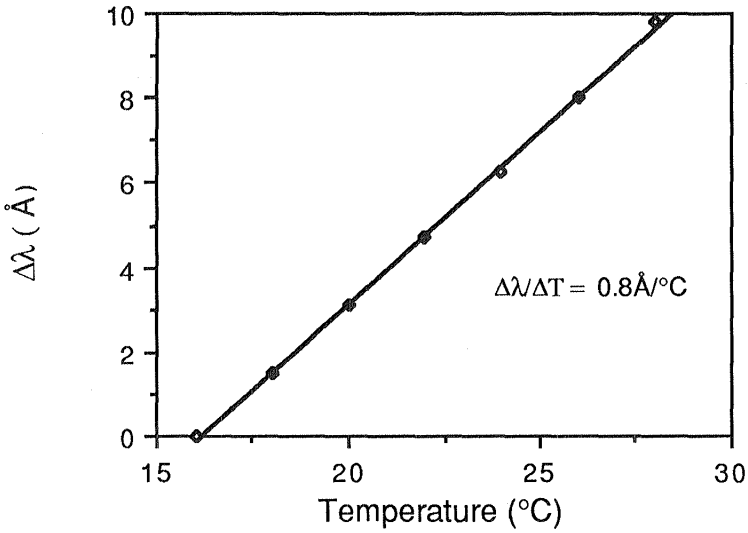

Figure 50. Change in output wavelength of a single-mode DFB laser as a function of heat sink temperature (wafer #QAL-1195). The wavelength at 16°C was about 1.291 μm.

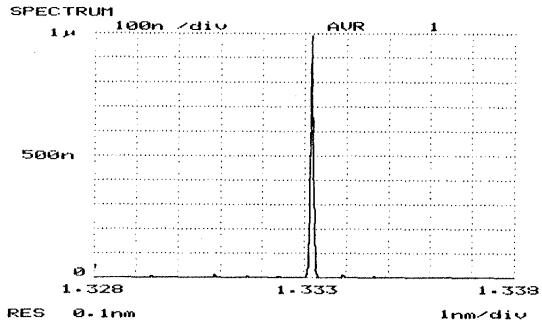

100 mA cw, linear scale

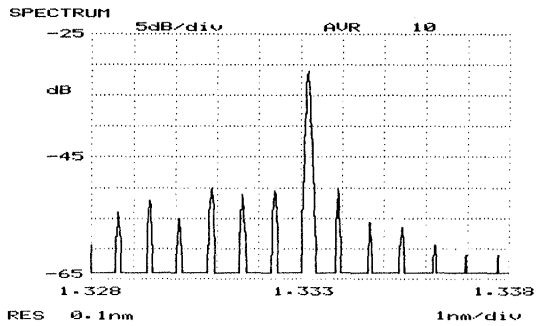

same, logarithmic scale

Figure 51. CW spectral emission of a DFB laser on linear and logarithmic scales, using an Anritsu spectrometer (wafer #QAL-1107).

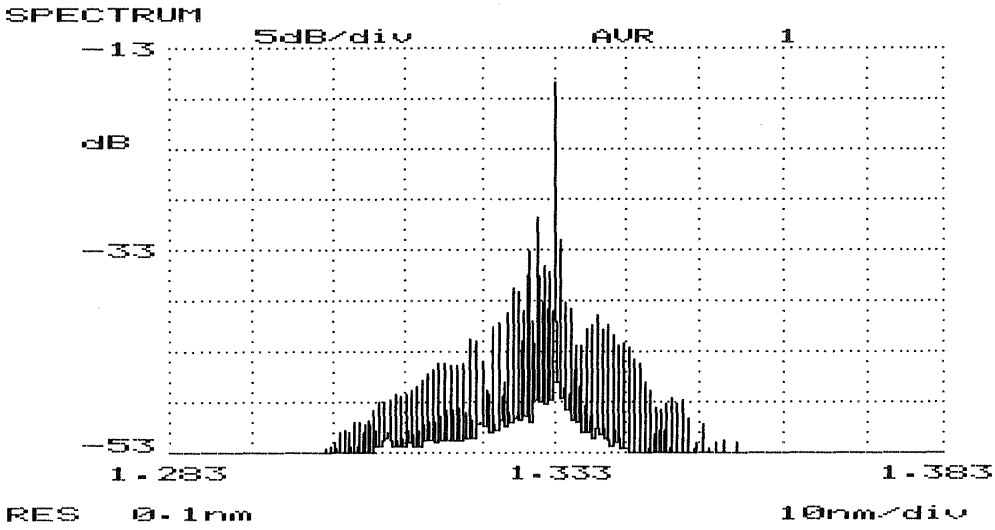

86-mA bias, 25-mA pulse amplitude
100-ns pulse length, 10% duty cycle

Figure 52. Spectral emission of a laser similar to the one in Fig. 51 under pulse excitation (wafer #QAL-1107).

Figure 51 displays the spectrum of such a laser recorded on linear and logarithmic scales, using an Anritsu grating spectrometer. The nearest side band is about 20 dB down in output power. When the laser is driven with 100-ns pulses, the rejection of the nearest side lobe is again about 20 dB (Fig. 52).

A typical far-field, shown in Fig. 53, indicates a beam of 54° in the transverse direction, and 15° in the lateral direction. A calculation of the far-field for this structure (Fig. 54) indicates a 57° beam in the transverse direction, which, considering the uncertainties in the layer thicknesses, is a very good agreement. Thus, the large beam angles for this direction are a consequence of the choice of layer thicknesses.

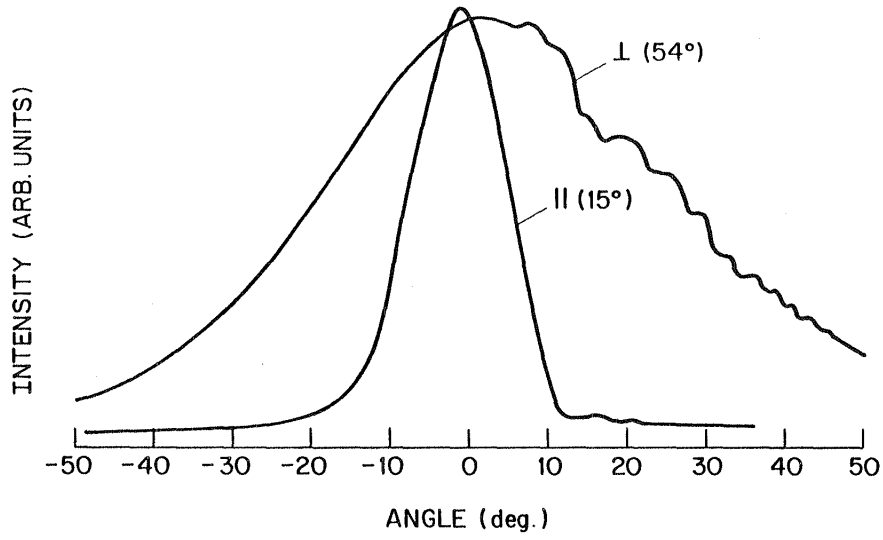

Figure 53. Measured far-field pattern of typical DFB laser.

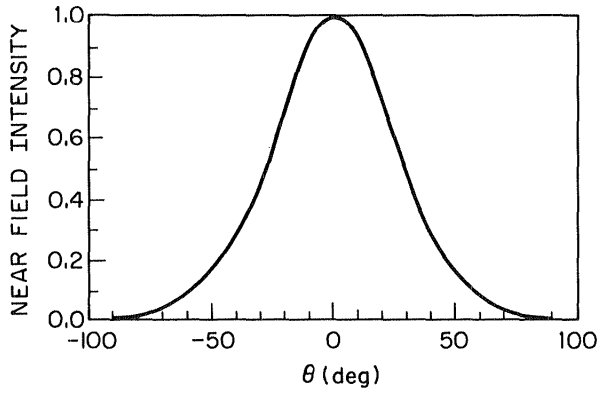

Figure 54. Calculated near-field pattern for structure equal to that measured in Fig. 53.

Going to a thinner active layer, on the order of 0.1 μm, provides a tighter far-field beam in the transverse direction. This is the trend to be followed for entirely different reasons, i.e., to get an improvement in the grating coupling coefficient and a reduction in the threshold current, both of which would result from thinner active layers. The transverse beam very likely can be brought down to the 30° range, but not to the 15° value of the lateral beam, which results from the relatively wide 3.5-μm ridge used in these lasers.

A wide ridge is desirable for maximum power output, but a narrower ridge yields a lower threshold and operating current. With a thinner active layer and a narrower ridge, beam angles of from 20 to 30° in both planes should be achievable. Making the ridge narrow (Fig. 55) leads to a new problem. The effective index in the region of the grating now depends on the ridge width. This is illustrated in Fig. 8 which shows how the calculated effective index for a 1.55-μm structure varies with the ridge width. Below about 3 μm, this effect must be included in the computation of the effective index and the grating period.

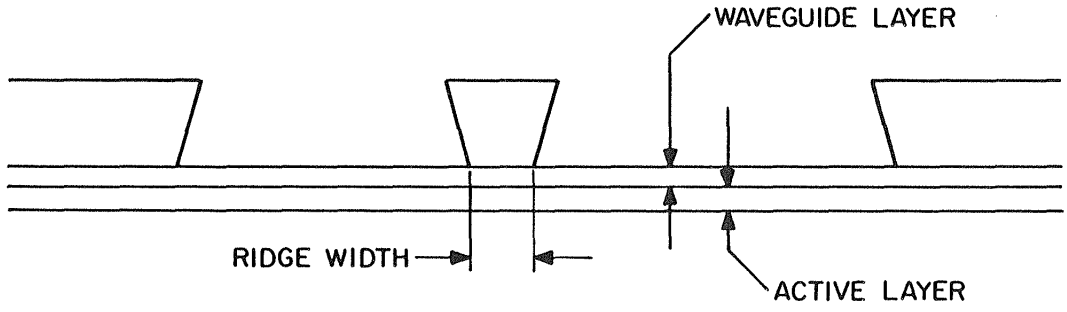

Figure 55. Schematic of a ridge-guide laser, illustrating the definition of ridge width.

In a standard DFB laser, a number of modes are allowed. They are disposed symmetrically about the Bragg frequency and have a threshold gain that increases with separation from the Bragg frequency (Fig. 56 a). Thus, in the ideal case, the two lines nearest the Bragg frequency will be excited, providing two-line emission. In practice, however, one often sees single line emission, which can be accounted for on the basis of several mechanisms.

The first arises from the possibility that the gain curve peak may not be located exactly at the Bragg frequency (in fact, it generally is not). Thus, one or the other line will have a lower threshold gain and will be excited preferentially (Fig. 56 b). This mechanism is rather weak, and the stability of lasers relying on it exclusively is not high. A more powerful selection mechanism is radiation loss [17], which produces a much reduced threshold gain for one or the other of the two lines nearest the Bragg frequency. The existence of this mechanism requires that some radiation be coupled out of the active layer, at 90° for the case of a second-order grating, and it is not possible to use a first-order grating. In all the above structures, the facet is assumed to be nonreflecting. Another mechanism leading

to single-line emission is a loss of grating periodicity. This no doubt occurs inadvertently on occasion, but is more appropriately introduced by a deliberate phase shift in the structure. In such a case, the emission (Fig. 56 d) occcurs in the forbidden band, exactly at the Bragg frequency [8].

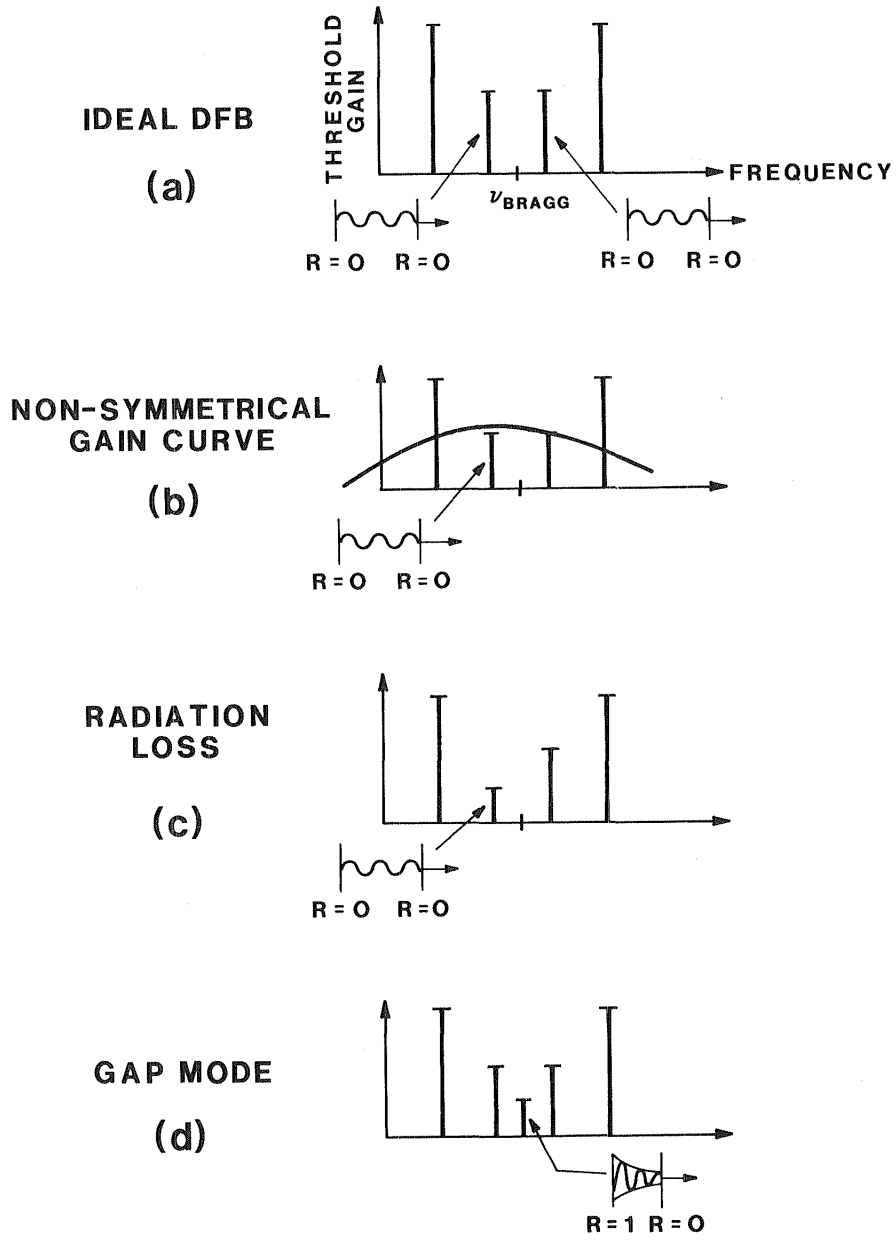

Figure 56. Schematic diagram illustrating the various spectra obtainable from ideal DFB lasers. (The meaning of these figures is explained in the text.)

There are a number of ways of introducing a phase shift, namely by varying the ridge width and thus the mode index along the cavity, by stitching the grating together out of sections having the same period but different phases, or by the phase shift resulting from reflection at a facet.

It appears that there are real advantages in making the laser with a first-order grating, and a phase-shift section. In that case, it is possible to use a triangular-etched grating, which, as pointed out above, is a self-limiting configuration, and thus is not sensitive to fabrication parameters. Furthermore, the coupling is always stronger with a first-order grating. For optimum output, this structure should have a 100% (nominal) reflector on the back facet, and an antireflection coating on the front facet.

XII. DFB MODULATION STUDIES

In addition to the optical characterization of the DFB lasers described earlier, the modulation bandwidth of some DFB lasers was measured. As already discussed, the ridge-guide structure was chosen over buried heterostructures, such as the buried crescent, because we felt it should have a better high-frequency response. A schematic of the setup used to characterize the frequency response of the DFB lasers is shown in Fig. 57. Briefly, the diode is biased with a dc current somewhat over the lasing threshold, and a small (a few mA) sinusoidal modulation is applied to the device through a microwave network. A drawing of this laser fixture, with a strip-line, bias tee network and the L-mount on which the diode is mounted, is shown in Fig. 58. The laser output is then coupled into an optical fiber about 1-m long, the output of which is butt-coupled to a InGaAs PIN photodetector package in a high-speed (> 3 GHz) detector module.

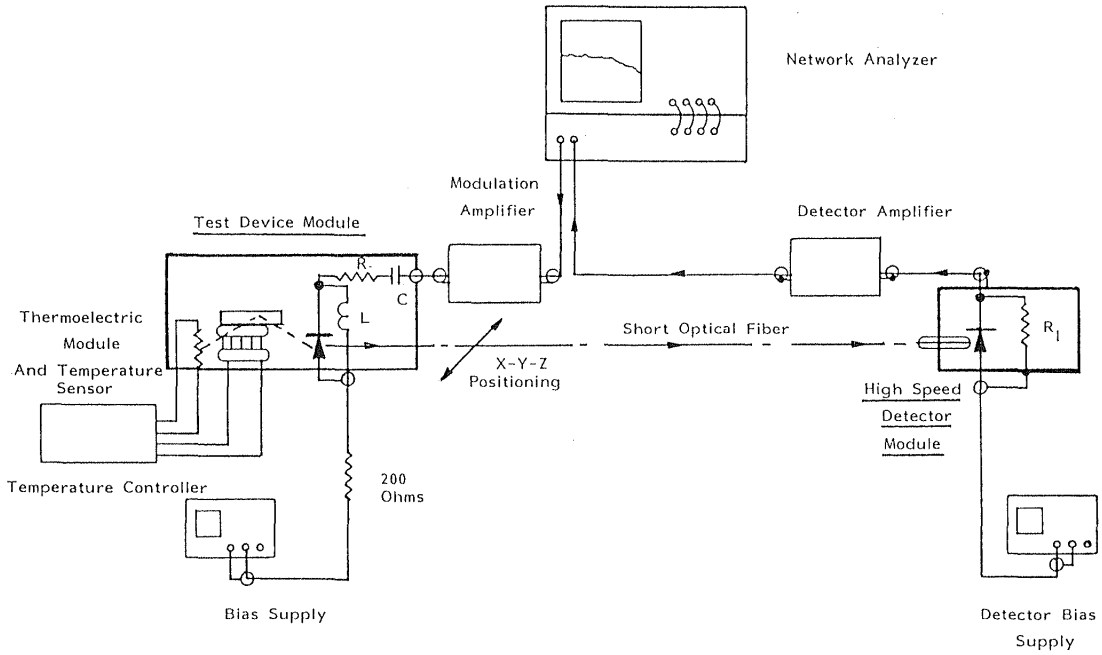

Figure 57. Schematic of the setup used to characterized the frequency response of DFB lasers.

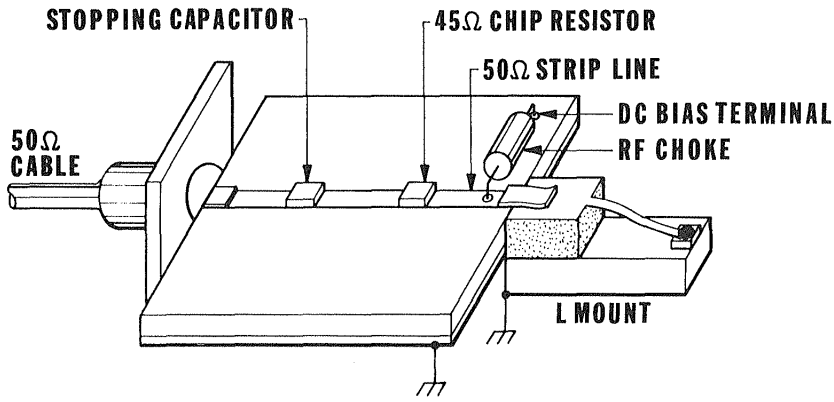

Figure 58. Laser fixture with strip-line, bias tee network, and L-mount used for high-frequency measurements on DFB lasers.

The measured frequency response of a ridge-guide DFB laser at two different bias levels is shown in Fig. 59. The threshold current for this device was about 65 mA. We see that at 100-mA bias, the 3-dB frequency response is about 2 GHz. However, some resonance effect around 1 GHz is apparent, and would degrade the performance of this device in a high bit-rate system.

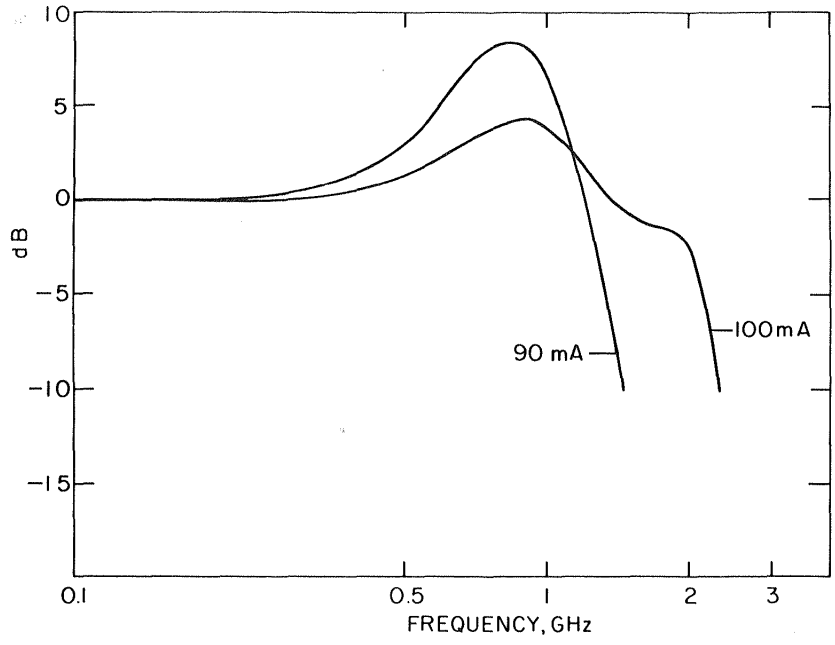

Figure 59. Frequency response of a DFB laser at two different bias levels.

The deleterious effects of this resonance can be seen by looking at the device output under digital modulation. This is shown in Fig. 60 for a 2-Gbit/s modulation. Fig. 60 (a) shows the electrical pulse from the word generator, and Fig. 60 (b) shows the light output from the laser at the same data rate. Significant distortion of the waveform is readily apparent in the figure.

This resonance effect is not completely understood. The most likely explanation is that it is caused by inductive effects in the L-mount, and is not inherent in the diode itself. Detailed measurements of the impedance of the L-mount as a function of frequency have been made, and a copy of a report describing the results is attached to this report as Appendix A. These characterization studies of the L-mount indicate that at 2 GHz the inductance of the L-mount contributes significantly to the impedance of the load. A modified L-mount designed to reduce this inductance is also described in Appendix A.

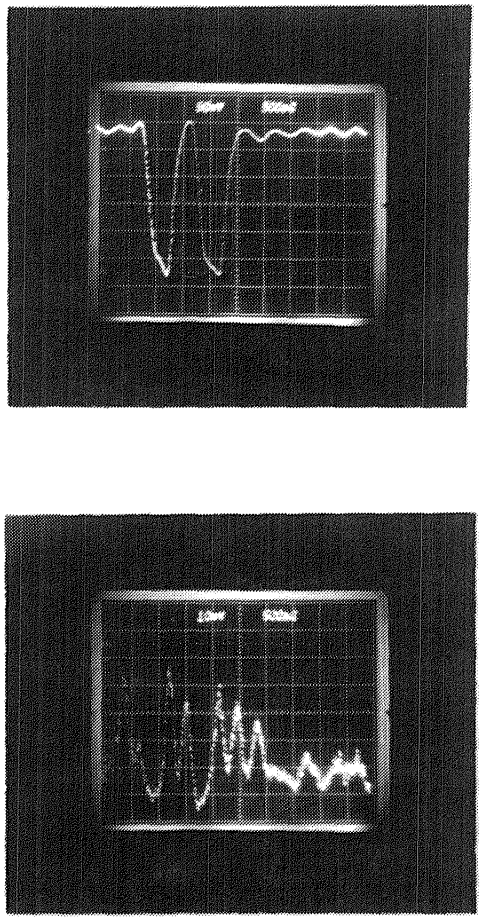

Figure 60. Digital modulation of ridge-guide DFB lasers at 2 Gbit/s; (a) shows the electrical pulse from the word generator for a 101000 pattern and (b) shows the light output from the laser for a 10101100 pattern. The dc bias on the laser was 130 mA.

XIII. HIGH-SPEED DFB PACKAGE

The development of a high-speed laser package with a fiber pigtail had two objectives: (1) to overcome the limited bandwidth of the L-mount and (2) to provide a rugged package suitable for incorporation into a fiber-optic system, which would serve as a prototype for a commercial package.

Several schemes were considered for optimizing the coupling between the laser and the fiber. The chosen design used a commercially available end-melt microlensed fiber. Measurements made on coupling a ridge-guide DFB laser to a lensed 1.3-μm single-mode fiber are shown in Fig. 61 (a - c). The total coupling efficiency for these lasers was in the range from 30% to 40%. Figure 61 shows that in the most critical direction (vertical, or perpendicular to the p-n junction) the tolerance at the half-power point is about 2 μm. Furthermore, the use of a lensed fiber allows these high coupling efficiencies at relatively large separation between the fiber and laser facet (17 μm). In butt-coupling with a cleaved fiber, there is a great risk of damaging the laser or fiber facet if they are bumped when trying to optimize the coupling.

Two other methods were considered for coupling the laser and fiber. The first was to use a fiber with an elliptical microlens. In principle, this elliptical lens should correct for the difference in the mode aspect ratio between the laser and the fiber. Fibers with such an elliptical lens have been fabricated at the David Sarnoff Research Center, but, to date, coupling experiments have been disappointing. The other problem with this technique is that if this package was to serve as a commercial prototype, it was important to use a commercially available fiber.

The second technique considered was to use two lenses between the laser and the fiber. This technique has the advantage that it is very tolerant of misalignment. However, it is difficult to assemble because of the large number of degrees of freedom, and it is difficult to implement in a rugged package. A technical report describing this two-lens technique appears in Appendix B.

In the designed package, the lensed fiber and laser were mechanically coupled by soldering the fiber into an Ni tube and soldering the Ni tube into the package after making a rough alignment. The final alignment was then accomplished by bending the Ni tube. The difficulty with this technique was that the Ni tube did not bend easily, and it was necessary to first overbend it to optimize

the coupling. Also, the long term stability of the coupling using this method was only about 90 days, which is unsatisfactory for any commercial device. This stability problem was probably due to deformation of the solder holding the tube.

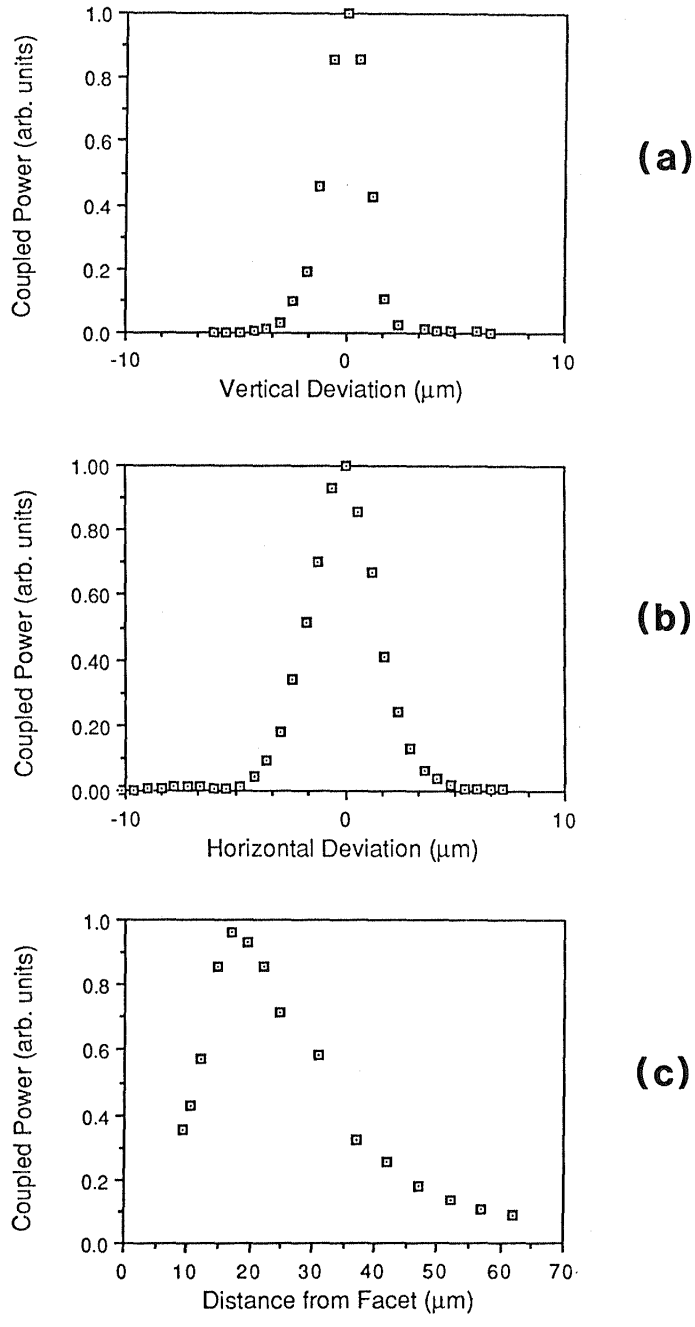

Figure 61. Measured coupled power from a ridge-guide DFB laser to a single-mode lensed fiber as a function of fiber position. A power unit of 1 corresponds to the same (arbitrary) power in each graph.

This fiber-coupling scheme has been transferred to RCA Electro-Optics, where the problems mentioned above have been solved. In particular, the tube has been altered to make bending easier, and the holder and soldering have been modified to improve the long-term stability. A picture of a fibered laser package fabricated at RCA Electro-Optics, which uses this coupling technology, is shown in Fig. 62.

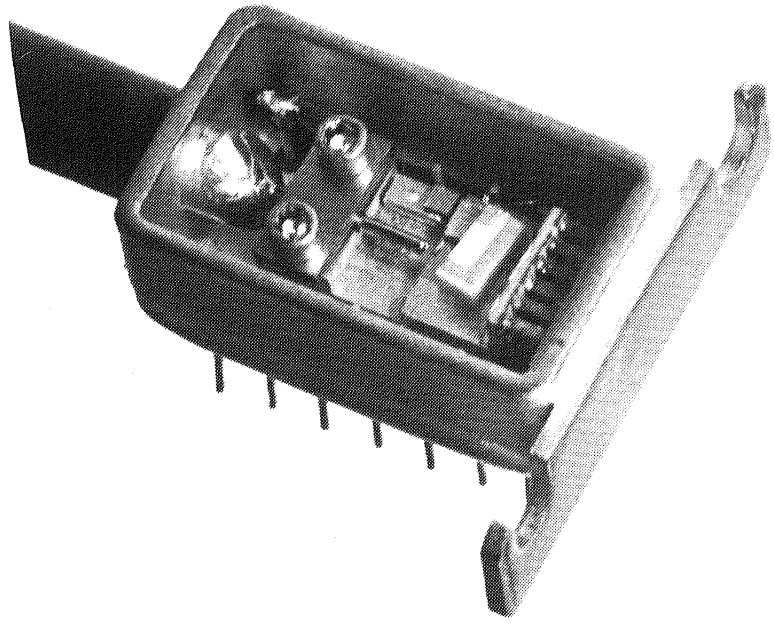

Figure 62. Fiber-pigtailed 14-pin DIL package designed and fabricated at RCA Electro-Optics.

The approach taken for the high-frequency design of the package was to bring the rf signal in using a 50-Ω strip line and then connecting the laser to the strip line. This is conceptionally similar to the L-mount fixture. To increase the bandwidth beyond what was otained with the L-mount fixture, it is necessary to minimize the parasitic inductance and capacitance associated with connecting the diode to the strip line. The most important consideration is to minimize the length of any lead wires.

the diode to the strip line. The most important consideration is to minimize the length of any lead wires.

Another consideration is how to drive a low impedance load (a few Ω) from a 50-Ω network effectively. The usual procedure is to build out the impedance of the diode using a 45-Ω chip resistor very close to the diode, which effectively terminates the transmission line at approximately its characteristic impedance. The problem with this approach is that the resistor consumes a large fraction of the oscillator power. This leads to both inefficient operation and possibly heating of the diode.

As an alternative, it was decided to use an impedance mismatched scheme in which the diode is connected directly across the transmission line. Provided the oscillator can effectively drive a load with this large a VSWR, this method is four times more efficient than using a build-out resistor. Also, provided the source and transmission line are matched, so that all reflections from the load are absorbed by the source, the frequency response of this network is flat for a resistive diode load. Of course at higher frequencies the reactance of the diode becomes important, and the frequency response will begin to roll off. The measured bandwidth will, however, be the same in both the matched and mismatched cases.

A third design possibility was to use a quarter wavelength strip line peaking equalizer circuit. This introduces a moderate peak on the frequency performance, which increases the response at high frequencies. This partially cancels the roll-off due to capacitive effects at high-frequency. A description of this method is in Appendix C. The limitation of this technique is that it is only effective for extending the frequency response when one is limited by a capacitive-like roll-off. For the DFB lasers, in which we expect to be limited by relaxation oscillations, the frequency response cannot be extended using a simple equalizing ciruit.

A picture showing the final design of the rf part of a prototype package is shown in Fig. 63. The rf signal is brought up to the laser from the edge of the package using a flexible 50-Ω strip line. This strip line is then connected to a bonding pad within a couple of millimeters of the chip, and the final connection is made with a small bond wire.

To test the bandwidth of this package, a high-speed laser was mounted and tested. A schematic of the rf network and test setup is shown in Fig. 64. The laser was a buried-crescent laser in which isolation channels had been etched to reduce

the effective chip area to about 30 x 200 μm. This reduced area minimized the capacitance due to the reverse biased junction, which limits the high-frequency response of the standard buried-crescent laser to several hundred MHz.

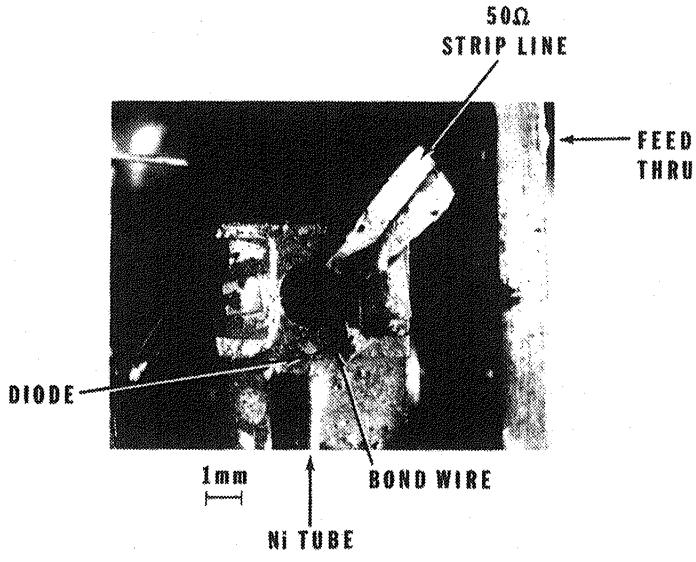

Figure 63. Picture of the high-frequency package showing the rf network.

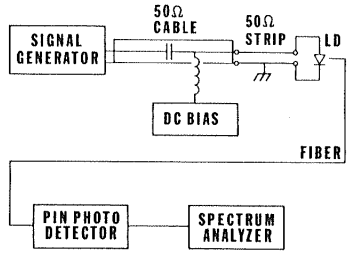

Figure 64. Schematic of the rf network used in the high-frequency package and the system used to characterize its bandwidth.

The frequency response of an etched-channel buried-crescent laser is shown in Fig. 65 for two different bias levels. The "error bars" indicated in the figure are included to show the peak to peak modulation (ripple) in the measured response. This ripple was a result of feedback from the fiber and does not affect

the basic measurement. The measurement clearly shows a frequency response for this laser and package of 4 to 5 GHz at 50-mA bias (2 times threshold).

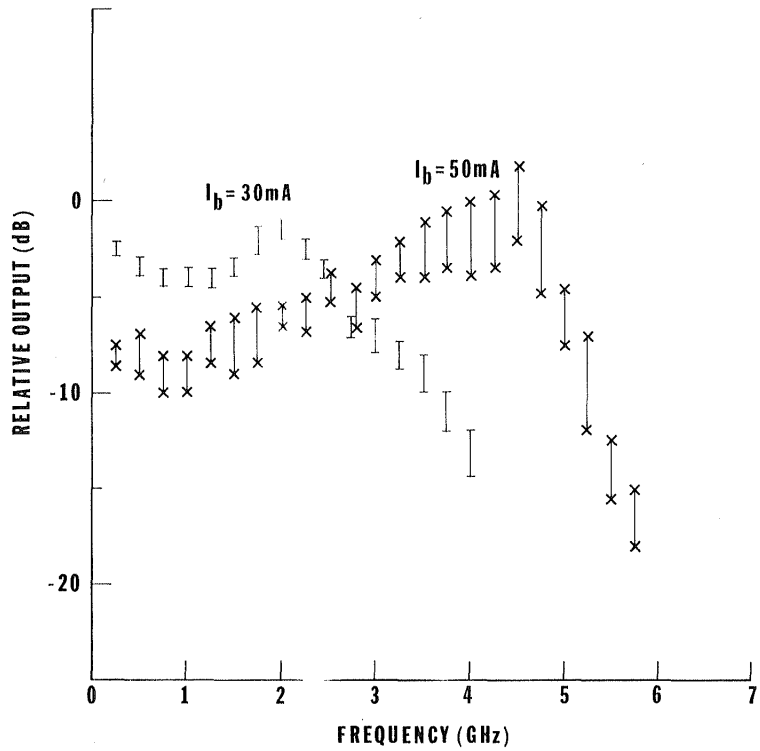

Figure 65. Bandwidth measurement of a high-speed, etched-channel buried-crescent laser in the high-speed package.

In summary, we have designed a pigtailed package for the DFB laser developed under this program, which is rugged and has a bandwidth exceeding 4 GHz. This package uses a lensed fiber, which is aligned by bending a Ni tube. The large bandwidth is obtained by bringing a 50-Ω strip line very close to the diode chip, and then minimizing the inductance of the bond wire. No impedance matching was used. Based on the results presented above, this package should serve as a useful prototype for a commercial package.

XIV. CONCLUSIONS

Successful single-mode InGaAsP lasers were fabricated using the ridge-guide DFB configuration. Various properties of these lasers were measured and calculated. Thresholds as low as 60 mA at room temperature with a sidemode suppression of 20 dB was obtained.

A number of possible improvements were discussed that could enhance the performance of these devices. For example, lower thresholds should result from minor changes in the structure, particularly the reduction of active-layer thickness from 0.2 μm to 0.1 μm. Modification in the layer thicknesses and ridge width could also be made to optimize the coupling to single-mode fibers. In addition, optimizing the grating design, probably using a first-order grating of triangular cross-section should reduce the threshold as well as improve the sidemode rejection. Incorporation of a phase shift in the grating would also be useful to increase the yield and sidemode suppression of single-mode devices.

It is also fruitful to reconsider some of the device structures that were not pursued under this program for a variety of reasons. For instance, buried heterostructures may have some advantages over the ridge-guide, both because of the low threshold current and the output power. In fact, as of this writing, the David Sarnoff Research Center has developed, under a subsequent program, a new buried-ridge DFB laser, that has demonstrated output powers over 20 mW in a single DFB mode.

Finally, now that DFB lasers have been developed at a number of places and are a well-established technology, we must direct our attention to the next technology. One of the most exciting areas in optical communications is coherent communications. To realize this technology, however, it is necessary to develop diode lasers that are highly coherent (i.e., have a narrow spectral linewidth).

Although DFB lasers have been shown to have narrower linewidths than Fabry-Perot lasers, the standard DFB still does not satisfy many of the requirements of coherent systems. Through modifications of DFB lasers that have been developed at the David Sarnoff Research Center and elsewhere, it may be possible to meet the needs of these applications. Extensions of the DBR laser structures should also be considered. In either case, the development work carried out under this program has given us a valuable step towards developing monolithic, narrow linewidth diode laser sources.

REFERENCES

1. G.P. Agrawal, "Lateral analysis of quasi-index-guided injection lasers: transition from gain to index guiding," IEEE/OSA Journal of Lightwave Technology LT-2, 537 (1984).

2. H. Ando, N. Susa, and H. Kanbe, "Carrier density profiles in Zn- and Cd-diffused InP," Japanese J. Appl. Phys. 20, 197 (1981).

3. C. Artigue, Y. Louis, P. Poingt, D. Sigogne, and J. Benoit, "Low threshold, second order DFB laser emitting at 1.3 μm for high bit-rate applications," IOOC-ECOC, 5th Int. Conf. Integrated Optics and Optical Fiber Comm., Venice, Italy, 1985, Tech. Dig. 1, 33.

4. N. Chand and P.A. Houston, "Diffusion of Cd and Zn in InP between 550 and 650°C," J. Electronic Materials 11, 37 (1982).

5. A.K. Chin, B.V. Dutt, H. Temkin, W.A. Bonner, and D.D. Roccasecca, "Formation of p^+-p^--n^--junctions in InP by Cd diffusion," Appl. Phys. Lett. 36, 924 (1980).

6. B. Cockayne, W.R. MacEwan, G.T. Brown, and W.H.E. Wilgoss, "A systematic study of the electrical properties of Fe-doped InP single crystals," J. of Materials Science 16, 554 (1981).

7. B.V. Dutt, A.K. Chin, and W.A. Bonner, "Diffusion of Cd into InP at 680°C," J. Electrochemical Society 128, 2014 (1981).

8. C.H. Henry, "Performance of distributed-feedback lasers designed to favor the energy gap mode," IEEE J. Quantum Electronics QE-21, 1913 (1985).

9. C.H. Henry, L.F. Johnson, R.A. Logan, and D.P. Clarke, "Determination of the refractive index of InGaAsP epitaxial layers by mode-line luminescence spectroscopy," IEEE J. Quantum Electronics QE-21, 1887 (1985).

10. H. Kogelnik and C.V. Shank, "Coupled-wave theory of distributed-feedback lasers," J. Appl. Phys. 43, 2327 (1972).

11. W. Kubert, O. Hildebrand, H.W. Marten, and N. Arnold, Inst. Phys. Conf. Ser. No. 65, Int. Symp. GaAs and Related Compounds, Ch. 7, 597, Albuquerque, NM (1983).

12. I. Ladany and D.P. Marinelli, "Ohmic contacts for laser diodes," RCA Review 44, 101 (1983).

13. L. Lewin, "Obliquity-factor correction to solid-state radiation patterns," J. Appl. Phys. 45, 2323 (1975).

14. J. Manning and R. Olshansky, "The carrier-induced index change in AlGaAs and 1.3-μm InGaAsP diode lasers," IEEE J. Quantum Electronics QE-19, 1525 (1983).

15. T. Saitoh, "New chemical-etching solution for InP and GaInAsP gratings," Electronics Letters 18, 408 (1982).

16. R.B. Smith and G.L. Mitchel, EE Technical Report No. 26, University of Washington, Seattle, WA.

17. W. Streifer, R.D. Burnham, and D.R. Scifres, "Radiation losses in distributed-feedback lasers and longitudinal mode selection," IEEE J. Quantum Electronics QE-21, 737 (1976).

18. W. Streifer, D.R. Scifres, and R.D. Burnham, "Coupling coefficients for distributed-feedback single- and double-heterostructure diode lasers," IEEE J. Quantum Electronics QE-11, 867 (1975).

19. H. Temkin, G.J. Dolan, R.A. Logan, R.F. Kazarinov, N.A. Olsson, and C.H. Henry, "Ridge-waveguide, distributed-feedback lasers with electron-beam-defined gratings," Appl. Phys. Lett. 46, 105 (1985).

NASA
National Aeronautics and Space Administration

Report Documentation Page

1 Report No	2 Government Accession No	3 Recipient's Catalog No
NASA CR-4154		

4 Title and Subtitle	5 Report Date
Distributed Feedback Lasers	June 1988
	6 Performing Organization Code

7 Author(s)	8 Performing Organization Report No
I. Ladany, J.T. Andrews, G.A. Evans	RCA-PRRL-87-CR-3B
	10 Work Unit No
	506-44-21-01

9 Performing Organization Name and Address	11 Contract or Grant No
David Sarnoff Research Center Princeton, NJ 08543-5300	NAS1-17351
	13 Type of Report and Period Covered
	Contractor Report

12 Sponsoring Agency Name and Address	14 Sponsoring Agency Code
National Aeronautics & Space Administration Langley Research Center Hampton, Virginia 23665-5225	

15 Supplementary Notes

NASA-Langley Technical Monitor: H.D. Hendricks
Final Report - 6/19/84 - 6/19/86

16 Abstract

We have developed a ridge-waveguide distributed feedback laser in InGaAsP. These devices have demonstrated cw output powers over 7 mW with threshold currents as low as 60 mA at 25°C. Measurements of the frequency response of these devices show a 3 dB bandwidth of about 2 GHZ, which may be limited by the mount. The best devices have single-mode spectra over the entire temperature range tested with a side mode suppression of about 20 dB in both cw and pulsed modes. The design of this device, including detailed modeling of the ridge guide structure, effective index calculations, and a discussion of the grating configuration are presented. Also, the fabrication of the devices is presented in some detail, especially the fabrication of and subsequent growth over the grating. In addition, we have designed and tested a high-frequency fiber-pigtailed package, which is a suitable prototype for a commercial package.

17. Key Words (Suggested by Author(s))	18 Distribution Statement
Semiconductor lasers, ridge guide DFB lasers, single mode DFB lasers, LPE	Unclassified - Unlimited Subject Category 36

19 Security Classif. (of this report)	20 Security Classif (of this page)	21 No of pages	22. Price
Unclassified	Unclassified	86	A05

NASA FORM 1626 OCT 86

NASA-Langley, 1988

For sale by the National Technical Information Service, Springfield, Virginia 22161-2171

End of Document